U–Pb geochronology and zircon composition of late Variscan S- and I-type granitoids from the Spanish Central System batholith

David Orejana · Carlos Villaseca · Pablo Valverde-Vaquero · Elena A. Belousova · Richard A. Armstrong

Abstract The Spanish Central System (SCS) batholith, located in the Central Iberian Zone, is one of the largest masses of granite in the European Variscan Belt. This batholith is a composite unit of late- and post-kinematic granitoids dominated by S- and I-type series granite, with subordinate leucogranite and granodiorite. Zircon trace element contents, from two representative S-type and three I-type granitoids from the eastern portion of the SCS batholith, indicate a heterogeneous composition due to magma differentiation and co-crystallisation of other trace element-rich accessory phases. In situ, U–Pb dating of these zircons by SHRIMP and LA-ICP-MS shows 479–462-Ma inherited zircon ages in the I-type intrusions, indicating the involvement of an Ordovician metaigneous protolith, while the S-type intrusions exclusively contain Cadomian and older zircon ages. The zircon crystallisation ages show that these granites have been emplaced at ca. 300 Ma with a time span between 303 ± 3 Ma and 298 ± 3 Ma. Precise dating by CA-ID-TIMS reveals a pulse at 305.7 ± 0.4 Ma and confirms the major pulse at 300.7 ± 0.6 Ma. These ages match the Permo-Carboniferous age for granulite-facies metamorphism of the lower crust under the SCS batholith and coincide with a widespread granitic event throughout the Southern Variscides. Ti-in zircon thermometry indicates temperatures between 844 and 784°C for both the S- and I-type granites, reinforcing the hypothesis that these granites are derived from deep crustal sources.

Keywords U–Pb zircon dating · Peraluminous granites · Spanish Central System · European Variscan Belt

D. Orejana (✉) · C. Villaseca
Department of Petrology and Geochemistry (Complutense University of Madrid), Institute of Geosciences (CSIC), 28040 Madrid, Spain
e-mail: dorejana@geo.ucm.es

P. Valverde-Vaquero
Spanish Geological Survey, Madrid, Spain

E. A. Belousova
Department of Earth and Planetary Sciences, GEMOC, Macquarie University, Sydney, NSW 2109, Australia

R. A. Armstrong
Research School of Earth Sciences, Australian National University, Canberra, ACT, Australia

Introduction

Widespread granite magmatism is a common phenomenon in many continental collision zones. It usually occurs during late-orogenic crustal thinning and strongly overprints the previous metamorphic history. In this sense, precise dating of granites in this geodynamic setting can help to constrain the evolution of the continental crust during orogenesis.

The Iberian Massif is part of the European Variscan Belt. This collisional belt resulted from the oblique collision of Gondwana and Baltica–Laurentia during the Early Devonian to Mid-Carboniferous (e.g. Matte 1986, 2001). The Central Iberian Zone (CIZ; Julivert et al. 1972) represents the innermost region of the Iberian Massif. This zone is characterised by large volumes of granitic intrusions outcropping from central Spain to the NW of the Iberian Peninsula (Fig. 1). Initial attempts to date the Variscan plutonism in the CIZ by Rb–Sr and K–Ar techniques provided a wide age range from 360 to 280 Ma (e.g. Serrano Pinto et al. 1987; Villaseca et al. 1995). Recent precise U–Pb studies have constrained the age range to a

narrow span between 325 and 280 Ma (U–Pb zircon dating via TIMS or SHRIMP; e.g. Dias et al. 1998; Fernández-Suárez et al. 2000; Valle Aguado et al. 2005; Zeck et al. 2007b; Solá et al. 2009; Díaz-Alvarado et al. 2011). This time range coincides with other parts of the Variscan belt (e.g. Finger et al. 1997; Ledru et al. 2001; Ballèvre et al. 2009). In the CIZ, the plutonic events are late- and post-kinematic (Ferreira et al. 1987). The Spanish Central System batholith (SCS batholith; Villaseca and Herreros, 2000) has a dimension of 250 km × 90 km, which makes it one of the largest late-/post-Variscan batholith in the entire Variscan belt.

This study has been focused on the eastern sector of the SCS batholith. We have sampled five representative granites ranging from I- to S-type peraluminous granites (Villaseca et al. 1998). In order to constrain the age of emplacement and the inherited zircons, we have used a combination of U–Pb CA-ID-TIMS, SHRIMP and LA-ICP-MS geochronology. The in situ dating techniques have the advantage of the fast data acquisition with the high spatial resolution, essential to unravel the inherited zircon component. The CA-ID-TIMS, on the other hand, allows to discriminate emplacement ages within a time span of 5 Ma, which otherwise would challenge the limits of precision and accuracy of the in situ techniques (see Black et al. 2004). The trace element composition of zircon analysed by LA-ICP-MS provides additional information on the magmatic evolution (e.g. Claiborne et al. 2006; Gagnevin et al. 2010). We have also used the Ti-in zircon thermometer to relate zircon crystallisation with magma temperature (Ferry and Watson 2007), and in this manner constrain the granite genesis. Our data constitute the first precise geochronology results on the magmatism in the eastern sector and add important information to constrain the age of emplacement of the SCS batholith and the crustal sources involved.

Geological and geochronological background

The Spanish Central System batholith is composed of more than 100 intrusive units that configure one of the largest exposures of granitic intrusions in the European Variscan Belt (Bea et al. 1999; Villaseca and Herreros 2000). These felsic magmas were emplaced into an Upper Neoproterozoic to Lower Palaeozoic sequence of metasedimentary and metaigneous rocks. According to their modal composition, these plutons can be classified mainly as granite sensu stricto, with minor proportions of leucogranites and granodiorites (e.g. Villaseca et al. 1998). Almost, all of them are peraluminous and display silica contents chiefly from 67 to 76 wt% (Villaseca and Herreros 2000). Variations in their mineralogy and degree of Al saturation have led to subdivision in several series: (1) S-type peraluminous cordierite-bearing granitoids, (2) I-type metaluminous amphibole-bearing granitoids and (3) transitional biotite granitoids of intermediate peraluminous affinity (Villaseca and Herreros 2000). The geochemical data do not display strong differences, but allow the distinction of crystal fractionation trends that rarely connect I-type granites with more differentiated S-type leucogranites (Villaseca et al. 1998). The relatively similar composition between SCS S- and I-type granites, both in major elements and isotopic ratios (Villaseca et al. 1998), likely reflects the stability of the melting conditions during granite genesis and the participation of similar source components (Villaseca and Herreros 2000). Nevertheless, various hypotheses regarding the origin of the SCS granitic batholith have been suggested: (a) hybridisation of crustal melts and mantle-derived magmas (Pinarelli and Rottura 1995; Moreno-Ventas et al. 1995); (b) crustal assimilation by mantle-derived magmas (Ugidos and Recio 1993; Castro et al. 1999); and (c) partial melting of essentially crustal sources, either from lower crustal derivation (Villaseca et al. 1998, 1999) or from mid-crustal levels (Bea et al. 1999, 2003).

These granitic bodies intrude into the metamorphic complexes of the Spanish Central System and locally into low-grade rocks. These metamorphic complexes constitute a high-grade infrastructure separated by major shear zones from a low-grade suprastructure (see Macaya et al. 1991). Most of the granitoids from the SCS batholith intrude after the main phases of ductile deformation in the infrastructure (D2–D3 deformation of Macaya et al. 1991), which are coeval with migmatisation, and low-pressure/high-temperature M2 metamorphism, after an initial M1 Barrovian metamorphic event (Macaya et al. 1991; Escuder-Viruete et al. 1998). Peak metamorphism is constrained at around 340–330 Ma (U–Pb mnz; Valverde-Vaquero 1998; Escuder-Viruete et al. 1998; U–Pb zrn SHRIMP, Castiñeiras et al. 2008), and the low-pressure/high-temperature metamorphism is constrained at 322–320 Ma (U–Pb mnz, xnt, ttn; Valverde-Vaquero 1998). The high-grade gneisses have provided Ar–Ar muscovite and K–Ar biotite ages of 314–310 Ma (Bischoff et al. 1978; Valverde-Vaquero et al. 2007), which reflect cooling below 350°C. The fact that these granites have intruded in shallow level, epizonal conditions (<2 Kb; e.g. Villaseca and Herreros 2000), and produced contact metamorphism in the high-grade gneisses, indicates that the country rock in the eastern sector of the SCS batholith was already cold at the time of intrusion. This intrusive event is late-/post-kinematic with respect to the local D4 phase of deformation, which is equivalent to the regional D3 phase of upright folding in the CIZ.

Many attempts have been made in order to determine the crystallisation ages of the SCS felsic magmas (Casillas et al. 1991; Moreno-Ventas et al. 1995; Pinarelli and

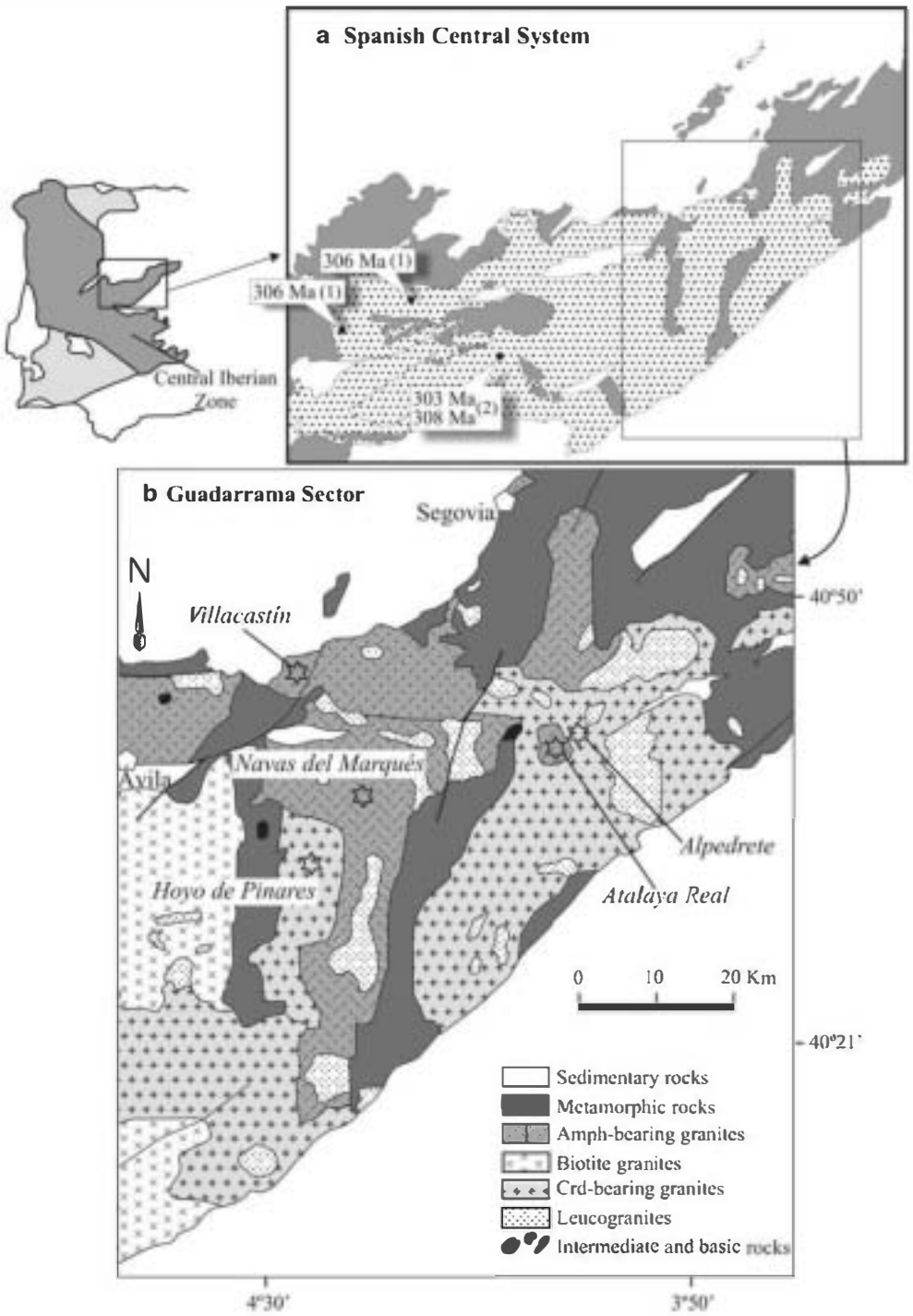

Fig. 1 **a** Sketch map of the Spanish Central System indicating available precise ages of granites from its western sector (*1* Zeck et al. 2007b, *2* Díaz-Alvarado et al. 2011). **b** Detail of the SCS eastern sector showing the main granitoid intrusions. *Stars* indicate the sampling location of the five plutons considered in the present study

Retura 1995; Villaseca et al. 1995; Bea et al. 1999). These studies were based on whole-rock Rb–Sr isochron and K–Ar in biotite analytical techniques, suggesting an extensive time period of 80 Ma for granite intrusion (360–280 Ma; see Bea et al. 1999; Villaseca and Herreros 2000 and references therein). In the western sector of the SCS batholith, recent U–Pb SHRIMP analyses on zircons yield ages in the 303–308 Ma range (Zeck et al. 2007b; Díaz-Alvarado et al. 2011). The data in the eastern end of the SCS batholith are limited to La Cabrera granite, which has been dated by Pb–Pb evaporation in zircon (301 Ma; Casquet et al. 2003) and U–Pb ID-TIMS in monazite (293 ± 2 Ma; Valverde-Vaquero 1998).

The scarce (~1%) coeval basic to intermediate magmas which accompany the granite intrusions are represented by small gabbroic to quartzdioritic plutons (Orejana et al. 2009; Scarrow et al. 2009). Single-zircon dating by TIMS yielded intrusion ages in the range 312–305 Ma for these

mafic bodies (Montero et al. 2004), but recent ion microprobe U–Pb zircon studies constrain the range to 307–300 Ma (Bea et al. 2006; Zeck et al. 2007b; Villaseca et al. 2011). The rest of igneous rocks cropping out in this region are restricted to post-orogenic dyke swarms of variable geochemical character (calc-alkaline, shoshonitic, alkaline and tholeiitic), which illustrates the transition to a rifting geodynamic setting from Upper Permian to Jurassic (Villaseca et al. 2004; Orejana et al. 2008). The intrusion of calc-alkaline porphyry dykes is poorly constrained around 290 Ma (Rb–Sr whole-rock isochron; Galindo et al. 1994), but data with higher accuracy confine the alkaline magmatism from 264 (Ar–Ar in amphibole; Scarrow et al. 2006) to 252 Ma (U–Pb in zircon; Fernández-Suárez et al. 2006), and the Messejana-Plasencia tholeiitic dyke to 203 Ma (Ar–Ar in biotite; Dunn et al. 1998).

Field relations and petrography

S-type intrusions (Alpedrete and Hoyo de Pinares)

These plutons outcrop along areas near 350 km^2 (Alpedrete) and 130 km^2 (Hoyo de Pinares) (Fig. 1) and show an irregular morphology due to emplacement of neighbouring younger granitic intrusions and tectonic contacts with the metamorphic wall-rocks. The development of contact aureoles is indicative of an epizonal emplacement level. They are mainly peraluminous medium-grained equigranular cordierite-bearing biotite granites and granodiorites. Leucogranites, which are also present in lower proportions, are generally interpreted as highly fractionated magmas derived from a monzogranitic parental melt (Villaseca et al. 1998 and references there in). Porphyritic textures with K-feldspar phenocrysts up to 4 cm long can be found locally. Rounded or elongated mafic microgranular enclaves (biotite-rich quartz-diorites to tonalites) are abundant and may appear dispersed or concentrated in bands, showing fine grain texture and size up to 50 cm. It is also possible to find schlieren structures, micaceous enclaves and metamorphic xenoliths. Plagioclase is usually idiomorphic and displays normal zoning; it can be altered to secondary muscovite, epidote and clinozoisite. K-felspar is also idiomorphic and, similarly to plagioclase, shows biotite and quartz inclusions. Biotite is an early crystallising mineral, being sometimes altered to chlorite and displaying a sagenitic texture, whereas muscovite is secondary and substitutes cordierite and feldspar. Cordierite appears as interstitial crystals highly transformed to pinnite. Its texture and composition suggest a magmatic origin (Villaseca and Barbero 1994). Typical accessory phases are apatite, zircon, monazite, xenotime, ilmenite and rare andalusite in aplopegmatitic varieties.

I-type intrusions (Villacastín, Navas del Marqués and Atalaya Real)

Villacastín and Navas del Marqués plutons are large, relatively irregular intrusions outcropping along 150 and 300 km^2, respectively (Fig. 1). They intrude in low-grade metamorphic rocks, inducing contact aureoles in the wall-rocks. The Villacastín granite seals the contact between the high-grade migmatitic gneisses and the low-grade rocks of the suprastructure (Macaya et al. 1991). The Atalaya Real pluton is a small rounded body within the Alpedrete granite (Fig. 1), and the contacts are not exposed so the relationship with the surrounding granite is uncertain. These I-type intrusions are mainly metaluminous to weakly peraluminous amphibole-bearing biotite granites and granodiorites, with minor leucogranitic facies. Similarly to S-type intrusions, mafic microgranular enclaves can be found in these I-type granitoids. Plagioclase shows oscillatory zoning and, together with biotite, is the main major early crystallizing mineral. K-feldspar is normally interstitial and may poikilitically include plagioclase, quartz and biotite. Amphibole is a green Mg-hornblende. Biotite is a good discriminant for SCS I-type granites as it plots in subaluminous fields below more Al-rich S-type biotites (Fig. 2 of Villaseca et al. 2009). Localised banding has been observed in Villacastín, whereas biotitic schlieren and metamorphic xenoliths near the contact are common in the three plutons. Flow textures appear in the most porphyritic facies. Occasionally, clinopyroxene (augite/diopside) is present as a residual mineral included in plagioclase or enclosed by amphibole. Apart from apatite, zircon, monazite, xenotime and ilmenite, other important accessory phases in these rocks are allanite, titanite and magnetite.

Field relations among the five studied intrusions are not straightforward. Nevertheless, according to its morphology and location, Atalaya Real seems to have intruded after Alpedrete pluton (Fig. 1). But both these granites are not in contact with the other three plutonic intrusions. Some deformation structures associated with the Variscan D4 deformation phase have been identified within the Hoyo de Pinares granite (Bellido et al. 1990), but they are rare in the Navas del Marqués and Villacastín granites. Accordingly, the Hoyo de Pinares granite was likely intruded by the Navas del Marqués pluton, whilst no clear relation exists between this latter intrusion and the Villacastín granite.

Sample preparation and analytical procedures

After standard separation techniques, a representative selection of zircons from each sample was handpicked and cast in epoxy resin for microanalytical analysis, together with some chips of reference zircons TEMORA 1 and

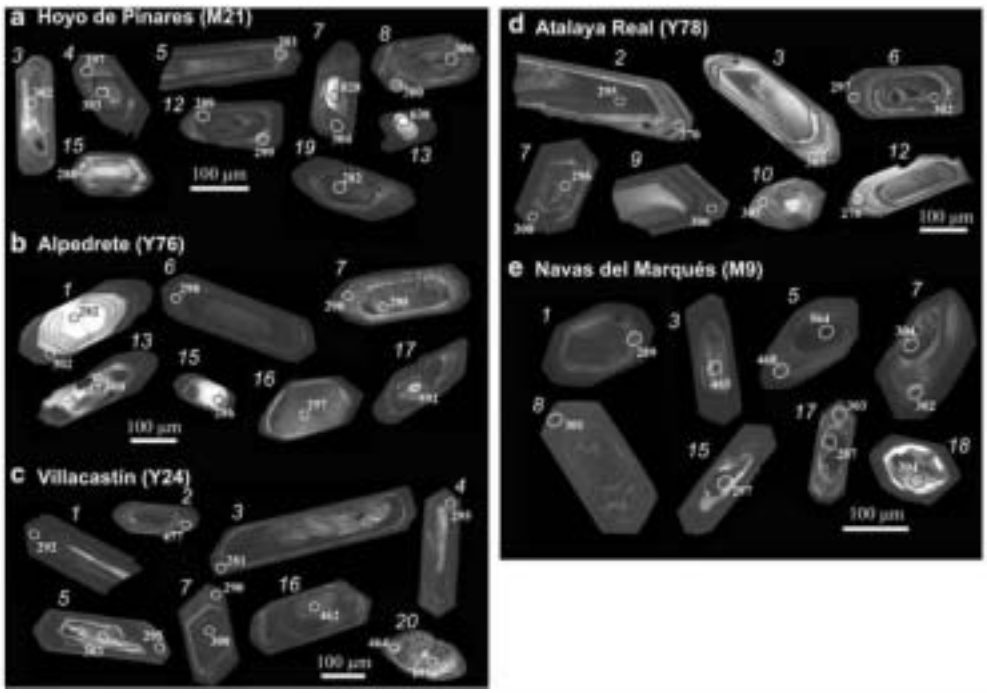

Fig. 2 CL images of representative zircon grains from the SCS granite intrusions with the analysed spots and concordia ages

SL13. The mount was ground down to expose the zircon central portions and imaged with transmitted and reflected light on a petrographic microscope, and with cathodoluminescence on a HITACHI S2250-N scanning electron microscope (housed at ANU-Canberra) to identify internal structure, inclusions, fractures and physical defects.

Selected areas in the grains were analysed for U, Th and Pb isotopes on the Sensitive High Resolution Ion Microprobe (SHRIMP II) at the Research School of Earth Sciences (Australian National University) with each analysis consisting of 6 scans through the relevant mass range. A 10-kV negative O_2 primary beam was focused to ~20 μm diameter. Positive secondary ions were extracted from the target spot of 0.5–1 μm deep at 10 kV and mass analysed at c. R5000 on a single ETP multiplier by peak stepping through the isotopes of interest. One TEMORA zircon standard was analysed for every three unknown analyses. Data were reduced following Williams (1998) and references therein, using the SQUID Excel Macro of Ludwig (2001), and Pb/U ratios were normalised relative to a value of 0.06683 for the $^{206}Pb/^{238}U$ ratio of the TEMORA reference zircon, equivalent to an age of 417 Ma (Black et al. 2003). Concentration data are normalised against zircon standard SL13 (210 ppm U, Black et al. 2004). Uncertainties given for individual analyses (ratios and ages) are at the 1σ level; however, uncertainties in the calculated concordia ages are reported as 95% confidence limits. Concordia plots were carried out using Isoplot 3.0 software (Ludwig 2003). Ages younger than 1,000 Ma are 204-corrected $^{206}Pb/^{238}U$, whereas one older age is 204-corrected $^{207}Pb/^{206}Pb$.

Alpedrete sample was also selected for new U–Pb age determinations performed on laser ablation ICP-MS at the GEMOC in the Macquarie University of Sydney. Analyses were carried out in situ using a New Wave 213 laser ablation microprobe, attached to a Agilent 7500 quadrupole ICP-MS. The laser system delivers a beam of 213-nm UV light from a frequency-quintupled Nd: YAG laser. Analyses were carried out with a beam diameter of 30 μm, a 5 Hz repetition rate and energies of 60–100 mJ/pulse. Typical ablation times are 100–120 s, resulting in pits 30–40 μm deep. The time-resolved signals were processed using the GLITTER interactive software to select the portions of the grains that had suffered least lead loss or gain of common Pb and were thus closest to being concordant. The standards used in this work are the GEMOC-GJ-1 with an age of 608.5 Ma, the Mud Tank zircon (734 ± 32 Ma; Black and Gulson 1978) and 91500 zircon (1,064 Ma; Wiedenbeck et al. 1995). Their measured mean values are within 2σ of the recommended values. Other analytical methods follow Jackson et al. (2004).

Several zircon fractions from Villacastín and Atalaya Real samples were selected for ID-TIMS and pre-treated with the chemical abrasion (CA) method of Mattinson (2005). We have selected this analytical method (which has higher accuracy than microanalytical techniques) with the aim of comparing the results with SHRIMP data, and get a more constrained age. Significant discrepancies between micro-analytical and ID-TIMS U–Pb data in Variscan granites have already been described (Teixeira et al. 2011). Zircon annealing was carried at 900°C for 48 h, and the chemical attack was done in Parrish-type minibombs inside

Parr bombs at 180°C for 12 h. Final zircon dissolution was achieved after placing the bomb at 240°C for 72 h. The procedure for extraction and purification of Pb and U is a scale-down version of that of Krogh (1973). A ^{208}Pb–^{235}U spike was used to obtain the U/Pb ratios by isotope dilution (ID) (Valverde-Vaquero et al. 2000). For test control, the 91500 (Wiedenbeck et al. 1995) and R33 zircon standards (Black et al. 2004) were dated with concordia ages of 1,065 ± 2.3 Ma and 419.7 ± 1.9 Ma, respectively. Isotopic ratios were measured with a Triton TIMS multi-collector mass spectrometer equipped with an axial secondary electron multiplier (SEM) ion counter. The instrument is set up to do measurements both in static and peak-jumping mode using the SEM. For static measurements, the ^{204}Pb was measured with the calibrated SEM (92–93% Yield calibration). The Pb measurements were done in the 1,300–1,460°C range, and U was measured in the 1,420–1,500°C interval. Data reduction was done using the PbMacDat spreadsheet (Isachsen et al. http://www.earth-time.org) and checked with PBDAT (Ludwig 1991). All isotopic ratios are corrected for mass fractionation, blank and initial common Pb after the model of Stacey and Kramers (1975). Ages and uncertainties were calculated with the decay constants of Jaffey et al. (1971) and are reported at the 2σ level; "concordia ages" were calculated with Isoplot 3.0 (Ludwig 2003).

Zircon trace element content was analysed using a New Wave 266 laser ablation microprobe coupled to the Agilent 7500 ICPMS system at the GEMOC. Analyses were carried with a 266-nm beam with a pulse rate of 5 Hz and energy of 1 mJ/pulse, producing a spatial resolution of 30–50 μm. The NIST-610 glass was used as the external calibration standard. The precision and accuracy of the NIST-610 analyses are 2–5% for REE, Y, Nb, Hf, Ta, Th and U at the ppm concentration level, and from 8 to 10% for Mn, P, Ti and Pb. Other analytical description has been given by Belousova et al. (2006).

Zircon description

Size, external morphology and inner texture of zircons from distinct S- and I-type granites have been studied by transmitted and reflected microscopy and CL imaging. A total number of 93, 84, 99, 65 and 120 grains have been considered, respectively, in the following samples: Hoyo de Pinares (M21), Alpedrete (Y76), Villacastín (Y24), Atalaya Real (Y78) and Navas del Marqués (M9). CL internal structure from representative grains is shown in Fig. 2. When viewed in transmitted light, zircons from all samples are similar in the usual presence of broken crystals, their euhedral to subhedral form, colourless to pale pink hue and abundant cracks and inclusions. They exhibit distinct primary morphologies: mainly elongated bipyramidal prisms with aspect ratios up to 1:8, but stubby prisms predominate in Villacastín (Y24) and Navas del Marqués (M9), and equant grains can be found in Atalaya Real (Y78). They show variable size, normally ranging from 80–100 to 450–500 μm, though in sample M9 and M21, they do not exceed 250 and 300 μm, respectively. A common feature of zircons from all samples is the presence of irregular cores separated from rims displaying CL zonation patterns by resorbtion surfaces (thin bright bands) (e.g. Fig. 2c, grain 7; Fig. 2e, grain 18). This texture appears associated with pre-Variscan and Variscan cores.

Sample M21 (Hoyo de Pinares)

CL textures are dominated by fine euhedral oscillatory zoning, with a progressively darker response towards crystal rims (Fig. 2a). Nearly, 40% of the mounted grains present some kind of inner core, though half of these are homogeneous and concordant, and appear to be an integral part of the oscillatory-zoned rim. The rest are irregular and display variable zoning patterns (oscillatory, convoluted, sector zoning) truncated by the zircon rim. These inner areas sometimes exhibit widening of the zoning bands and bright CL response.

Sample Y76 (Alpedrete)

CL internal structure is dominated by oscillatory rims and mantles, but darker outer rims are also common. Less than 30% of the grains have inner irregular cores. These are characterised by homogeneous dark CL response, wide bright bands or local recrystallisation. A few almost equant grains with a dark thin rim and homogeneous or sector-zoned core can also be found (Fig. 2b).

Sample Y24 (Villacastín)

According to CL imaging, elongated and stubby grains are characterised by oscillatory zoning. Independent of their habit, zircons may present texturally discordant cores with variable internal structures: oscillatory zoning, convoluted zoning and bright CL response (Fig. 2c).

Sample Y78 (Atalaya Real)

CL imaging reveals dominant oscillatory zoning in rims or the whole crystal (Fig. 2d). Widening of middle bright bands can occasionally appear. Zircon cores are usually homogeneous and concordant with the outer oscillatory zoning. Discordant corroded cores are rare and characterised by convoluted zoning or dark homogeneous CL response.

Sample M9 (Navas del Marqués)

Fine oscillatory zoning is the dominant internal structure. The most elongated prisms rarely show inherited cores, but these are common in the stubby zircons. Cores might be divided between (1) texturally concordant inner areas with bright CL response, widened oscillatory bands or convoluted zoning (Fig. 2e; e.g. grains 1, 18) and (2) irregular grains discordant with respect to the outer rim (Fig. 2e; e.g. grains 3, 15). The latter are sometimes isolated from the external zircon by a thin bright irregular band, and their internal structure is usually characterised by a dark response, either homogeneous or displaying convoluted or sector zoning.

Analytical results

Trace element composition

Table 1 reports selected zircon trace element analyses obtained by Laser Ablation ICP-MS from pre-Variscan inherited domains and Variscan zircons. A variety of CL textures have been chosen for analysis, which in most cases correspond with oscillatory-zoned rims or homogeneous and idiomorphic Variscan cores. All analyses (including inheritances) display large chemical variations ranging up to rather high concentrations: Hf (8,950–17,870 ppm), Y (760–5,000 ppm), U (92–3,500 ppm), Th (58–1,812 ppm), HREE (590–3,360 ppm), Nb (1–39 ppm) and Ta (0.32–12 ppm) (Table 1). Ti contents are relatively low, ranging mainly from 3.6 to 24.2 ppm.

Chrondrite-normalised REE patterns are also similar in all cases (S- and I-types), with much higher HREE contents with respect to LREE and typical negative Eu anomaly and positive Ce anomaly (Fig. 3a, b). Extreme LREE enrichment in 3 spots (Y24-02, Y24-09, M9-11) can be considered as anomalous values when compared with standard magmatic zircons (Hoskin and Schaltegger 2003). An evident similarity in composition exists between all Variscan zircons and older inherited cores, with the latter showing higher Nb and Ta values (Fig. 3d).

A positive correlation between Hf or U (both used in the figures as differentiation index) and Nb (Ta) (Fig. 3c), but negative with respect to Zr/Hf ratio (which ranges from 32 to 58) (Fig. 4), can be found for all Variscan zircons. On the other hand, the rest of trace elements behave differentially depending on the intrusion considered (Fig. 4). Navas del Marqués (M9) zircon is generally enriched in all elements towards higher Hf. Villacastín (Y24) and Atalaya Real (Y78) zircons show positive correlation for P, Y and HREE, whereas those from Alpedrete (Y76) and Hoyo de Pinares (M21) do not display a positive correlation neither for these latter elements nor for the LREE.

U–Th–Pb zircon geochronology

Ninety-four crystals were analysed by SHRIMP (19, 19, 22, 14 and 20 grains from samples M21, Y76, Y24, Y78 and M9, respectively), 21 of them in several places. In addition, 12 zircon cores from the Alpedrete (Y76) intrusion were analysed by Laser Ablation ICP-MS, resulting in a total of 127 in situ analyses (Table 2). CA-ID-TIMS was done in zircons from the Villacastín (Y24) and Atalaya Real (Y78) granites (Table 3). The data are plotted in Wetherill concordia diagrams with all error ellipses at 2σ (Figs. 5, 6, 7). Figure 2 shows representative CL images of crystals featuring location of the analysis craters and resulting ages. The in situ analyses yielded $^{238}U/^{206}Pb$ ages with relatively wide ranges. However, coherent concordia ages at 2σ confidence level have been calculated with Isoplot software using a selection of data (see "Discussion" for further details on the criteria of selection).

U and Th contents described bellow for all samples have been taken from the SHRIMP database, which is larger than the LA-ICP-MS data. Though some differences exist between both groups of analyses, Th/U ratios are generally similar irrespective of the technique considered. There is a chiefly continuous variation in U (74–2,037 ppm) and Th (25–1,067 ppm) contents. But much higher values (U = 2,000–6,000 ppm) can be found in a few analyses (Table 2). Th/U ratios are also fairly variable, ranging principally from 0.07 to 0.9.

Hoyo de Pinares granite

Twenty analyses from sample M21 provided Variscan ages, corresponding to oscillatory-zoned rims and inner cores with variable CL structure (leaving aside inheritances). Four partially corroded zircon cores revealed concordant or slightly discordant $^{238}U/^{206}Pb$ pre-Variscan ages (mainly Upper Proterozoic): 828 ± 9 Ma (7.2), 638 ± 9 Ma (10.1), 619 ± 8 Ma (13.1) and 369 ± 6 Ma (18.1). The three first inheritances have variable CL response (bright to pale bands), whereas the latter displays convoluted zoning and is characterised by high common ^{206}Pb contents.

The Variscan ages display error ellipses (2σ) overlaping the concordia curve to a greater or lesser extent (Fig. 5a). However, two analyses showing the highest degrees of discordance have not been considered for averaged age calculations (spots 6.1 and 17.1). Other data have also been rejected due to high U concentrations (analysis 1.1: 4,141 ppm) or common ^{206}Pb (spot 16.1). The remaining 16 analyses yield $^{238}U/^{206}Pb$ ages in the range 306–281 Ma, with a narrower selection providing a concordia age of 299.1 ± 1.8 Ma (MSWD = 0.99; n = 14) (Fig. 5b).

Table 1 Representative trace element composition (ppm) of zircon from SCS granitic intrusions determined by laser ablation ICP-MS

Sample	S-type granites									
	Hoyo de Pinares (M21)					Alpedrete (Y76)				
# analysis and description[a]	2.1 V	3.1 V	4.2 V	6.1 V	18 PO–I	1.2 V	4.1 V	L3 V	L4 V	17.1 PO–I
P	276	481	706	379	684	909	732	306	178	758
Ti	14.0	11.9	14.8	19.0	8.4	16.0	14.6	6.63	5.87	12.1
Y	814	2,021	2,221	1,104	2,041	3,483	3,780	3,652	2,014	2,902
Nb	1.21	2.93	3.07	1.16	3.18	2.09	4.56	2.07	1.81	3.19
Ta	0.87	0.63	0.80	0.39	3.03	0.90	2.41	0.49	0.51	1.04
Hf	14,450	10,958	13,106	11,570	13,221	17,864	13,178	10,388	11,577	16,842
Pb	0.76	4.33	6.04	3.13	2.22	1.66	27.0	6.02	3.84	3.93
Th	37.6	177	243	163	53.3	126	827	375	277	106
U	456	340	516	213	649	243	944	332	346	576
La	0.44	0.38	0.55	0.37	0.32	0.73	1.71	0.39	0.23	0.58
Ce	0.69	3.73	3.68	3.08	1.78	3.52	21.07	11.15	12.37	2.65
Pr	0.31	0.31	0.38	0.28	0.22	0.52	1.17	0.92	0.18	0.40
Nd	1.63	5.75	2.66	1.91	1.46	5.09	10.61	10.03	5.45	3.00
Sm	2.97	10.13	10.38	6.08	2.34	13.58	15.57	17.71	13.04	4.63
Eu	0.55	1.00	0.90	0.70	0.57	1.05	1.39	2.29	1.05	0.82
Gd	8.39	49.07	38.57	29.20	16.23	78.56	84.59	98.66	49.98	38.37
Tb	3.96	17.14	17.08	9.56	9.67	28.54	30.80	33.43	18.54	16.36
Dy	59.88	195.1	205.9	115.2	150.3	328.5	361.4	396.5	223.2	243.3
Ho	27.85	67.44	76.72	38.59	68.83	117.4	134.4	134.2	77.72	98.89
Er	149.0	302.1	345.2	166.5	357.4	493.8	550.6	554.6	316.5	468.5
Tm	37.48	60.06	73.64	35.31	84.00	100.9	110.2	107.3	64.47	107.1
Yb	380.1	562.7	684.7	331.0	863.3	913.4	968.4	969.2	572.5	1,074
Lu	77.44	105.5	122.1	57.99	160.1	163.7	178.4	159.6	92.74	195.3
T (°C)[b]	833	815	839	868	779	847	837	756	744	817

Table 1 continued

Sample	I-type granites												
	Villacastín (Y24)					Atalaya Real (Y78)			Navas del Marqués (M9)				
# analysis and description[a]	1.1 V	5.2 V	9.1 V	2.1 O–I	20.2 PO–I	2.2 V	3.1 V	13.1 V	7.2 V	11.1 V	15.1 V	5.1 O–I	5.2 PO–I
P	506	863	423	426	264	348	218	291	101	385	157	631	446
Ti	3.88	12.6	15.6	24.2	11.7	3.64	8.85	13.6	16.2	8.51	7.59	13.4	16.7
Y	2,574	4,796	4,095	2,136	2,484	1,830	1,166	893	1,030	2,841	1,620	2,213	3,474
Nb	6.52	4.00	11.6	20.3	11.8	3.15	2.01	1.04	2.85	16.7	3.10	11.2	38.8
Ta	4.49	2.13	7.71	11.8	3.96	2.07	0.86	0.32	1.22	6.93	1.25	2.55	12.0
Hf	14,510	16,240	14,687	13,168	16,131	16,189	10,833	11,202	8,954	12,857	9,543	12,713	12,617
Pb	24.3	10.4	41.7	44.4	30.9	4.26	2.70	1.05	2.82	46.3	8.92	5.58	20.8
Th	410	468	980	366	262	205	124	58.9	98.5	1,812	377	194	415
U	1,450	635	2,716	1,809	374	878	226	92.9	251	3,415	616	450	1,488
La	0.68	0.19	42.30	32.70	0.56	0.39	0.14	0.12	0.97	9.74	1.19	1.89	3.72
Ce	9.10	13.89	156.2	91.86	21.69	5.44	5.91	1.61	5.41	52.28	14.11	10.78	32.57
Pr	0.29	0.35	23.39	13.23	0.35	0.14	0.12	0.12	0.54	5.56	1.15	1.44	2.14
Nd	2.90	5.24	145.8	74.08	2.85	1.22	1.41	1.87	4.34	30.53	8.23	8.57	16.34
Sm	5.21	15.96	46.24	31.01	9.83	4.07	4.25	3.92	5.82	20.32	10.95	10.71	12.18
Eu	0.67	0.96	4.75	1.95	0.87	0.28	0.47	0.23	0.99	3.63	1.09	0.64	1.38
Gd	35.76	98.63	118.4	69.71	46.68	26.11	24.15	19.32	17.42	73.28	36.48	35.84	75.94
Tb	16.46	37.52	34.74	19.08	19.23	11.62	8.63	6.91	7.10	22.86	11.85	14.30	27.60
Dy	216.7	460.0	386.2	195.9	233.7	155.1	105.5	85.01	88.9	282.7	155.8	192.57	339.9
Ho	86.48	173.3	132.8	68.16	86.96	63.58	40.44	30.93	37.17	98.17	53.32	78.71	121.91
Er	406.0	721.4	587.1	301.5	369.2	302.2	182.8	136.1	161.1	413.8	254.3	337.56	536.5
Tm	90.57	154.5	126.8	70.17	79.61	67.09	38.39	28.60	36.62	89.08	59.71	76.59	115.8
Yb	889.5	1,445	1,193	720.2	738.0	678.4	371.5	265.6	361.1	912.1	597.8	707.91	1,064
Lu	149.6	225.2	202.5	126.7	124.9	112.3	61.55	45.96	71.39	135.3	93.64	116.07	144.3
T (°C)[b]	707	821	845	897	814	701	784	829	849	780	769	827	852

[a] *O–I* ordovician inheritance, *PO–I* pre-ordovician inheritance, *V* variscan zircon

[b] Temperatures estimated using the Ti-in-zircon geothermometer recalibrated by Ferry and Watson (2007). Temperature uncertainty for each data is ±4.5%

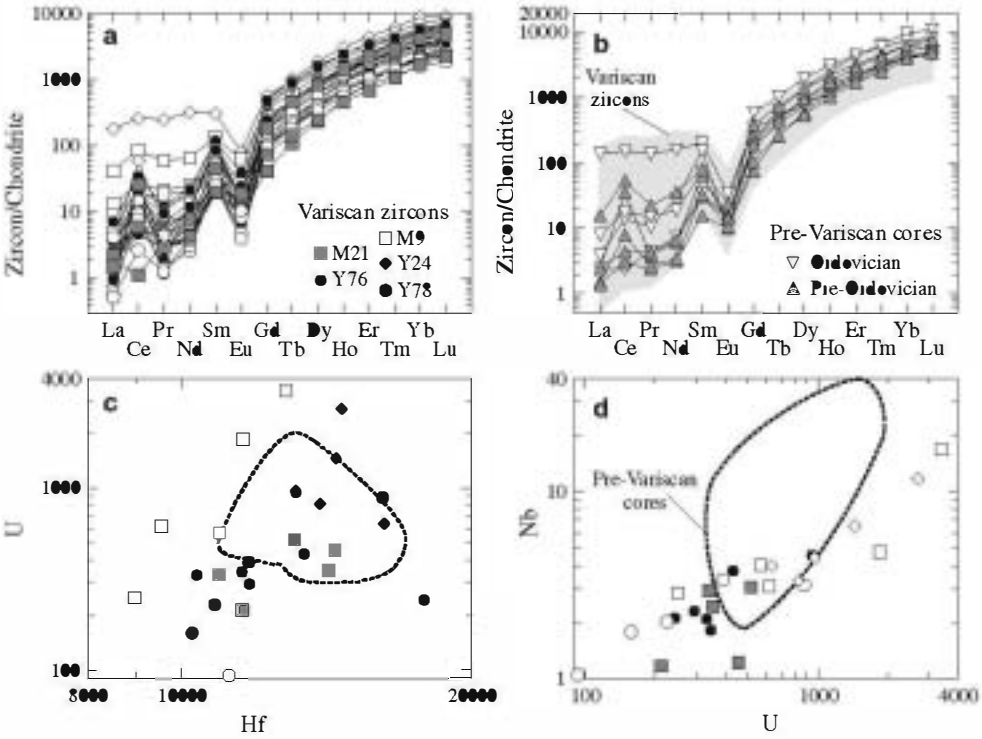

Fig. 3 Trace element composition of zircons from the SCS granites: Chondrite-normalised REE patterns of Variscan zircons **a** and pre-Variscan cores **b**, and U concentrations versus Hf **c** and Nb **d** contents. Normalising values after Sun and McDonough (1989)

Alpedrete granite

Almost all SHRIMP analyses from sample Y76 represent crystallisation ages. Only two inherited ages have been found in this sample corresponding to corroded cores with faint oscillatory zoning surrounded by dark homogeneous irregular domains, which provide concordant Neoproterozoic ages: 592 ± 7 Ma (analysis 17.1) and 581 ± 7 Ma (analysis L7). Exceedingly high common ^{206}Pb contents have been found only in one zircon core (spot 19.1).

The remaining analyses comprise a broad time span of 40 Ma with mostly concordant ^{238}U/^{206}Pb ages from 302 to 261 Ma (Fig. 5c). Th and U contents seem to correlate negatively with age for part of the data (not shown), probably suggesting some kind of secondary deviation of the calculated age. Analyses showing this behaviour (1.2, 2.1, 3.2, 4.2, 10.1, 11.1, 14.1 and 15.1) are seemingly concordant zircon cores with homogeneous bright CL luminescence, and display lower ages than their surrounding rims. Thus, we have not considered these latter data in averaged age calculations, together with other spots with high discordancy (16.1, 18.1 and 19.1). The resulting 12 spots range from 288 to 302 Ma. Seven of these analyses provided a concordia age of 297.1 ± 2.4 Ma (MSWD = 1.15) (Fig. 5d).

LA-ICP-MS analyses yielded 11 crystallisation ages (Table 2). Two of them (L6 and L11) are excluded due to high common Pb or degree of discordance. The remaining 9 analyses scatter in a range very similar to that shown by the SHRIMP results (Fig. 5e). A selection of six analyses provided a concordia age of 301.7 ± 3.4 Ma (MSWD = 2.7) (Fig. 5f), which overlap within analytical error with that calculated using SHRIMP data.

Villacastín granite

Sample Y24 yielded 22 Permo-Carboniferous ages from a total of 26 analyses. Four pre-Variscan ^{238}U/^{206}Pb ages have been found in three zircon grains. This pre-Variscan component is found in corroded cores with oscillatory zoning (sometimes partially convoluted) or decomposed zoning, enclosed by thin dark rims (Fig. 2c; grains 16 and 20). Three of these ages are Ordovician: 479 ± 5 Ma (2.1), 462 ± 5 Ma (16.1), 464 ± 5 Ma (20.1), and one is Lower Proterozoic, 1,956 ± 12 Ma (20.2), which corresponds to inheritance within an Ordovician core.

Some of the analyses of dark zircon rims and blurred inner domains (spots 1.1, 3.1, 6.1, 7.2, 8.1, 11.1, 12.1, 14.1, 17.1, 18.1, 19.1, 21.1) show high levels of common ^{206}Pb lead with exceedingly young ages (271–292 Ma). We have excluded these analyses and one spot with high discordancy (5.2) from averaged age calculations. The remaining 9 analyses, ranging from 288 to 300 Ma (Fig. 6a), correspond mainly with rims showing oscillatory zoning. The calculated concordia age for this sample yield 297.6 ± 2.8 Ma (MSWD = 0.16; n = 5) (Fig. 6b).

The four zircon fractions analysed by CA-ID-TIMS overlap concordia between 299 and 302 Ma and provide a

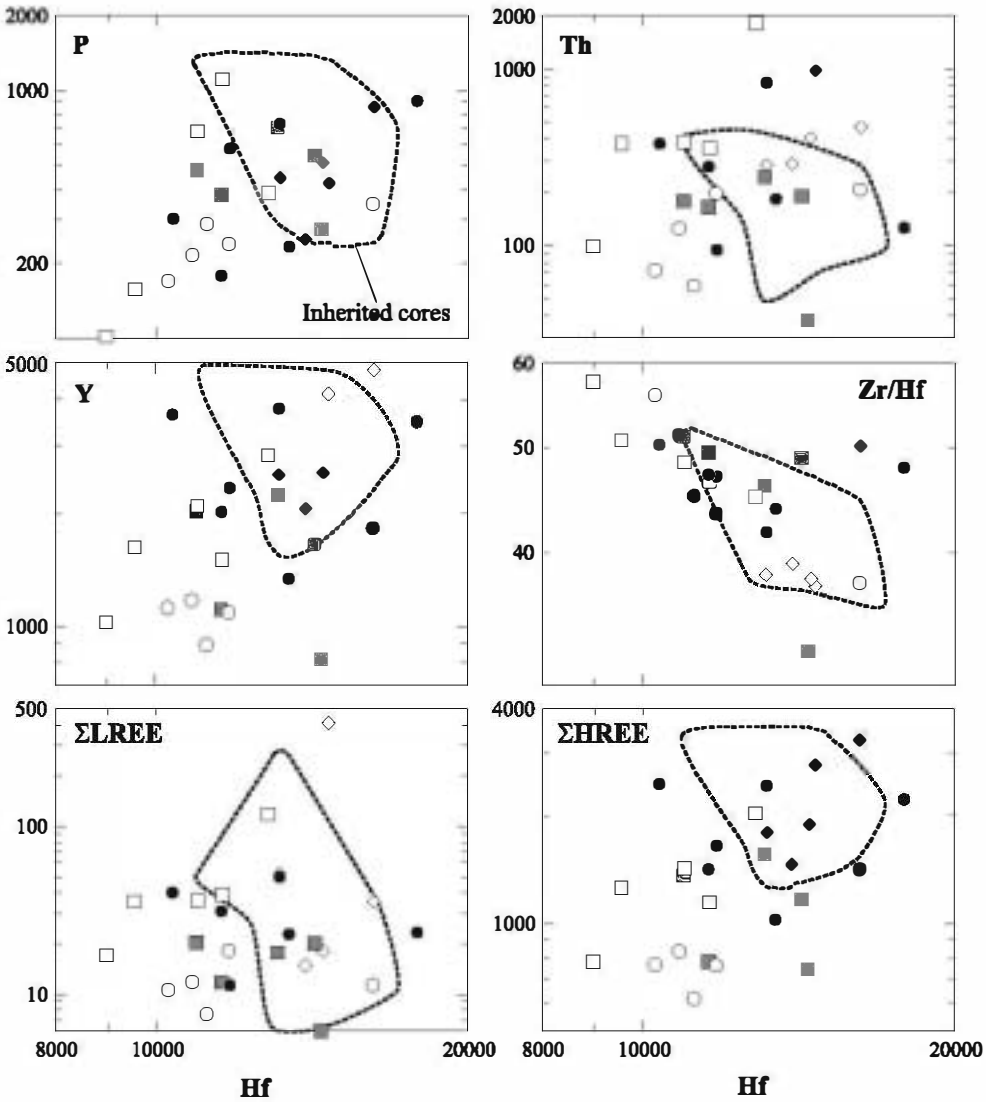

Fig. 4 Trace element composition of Variscan zircons from the SCS granites. Hf concentration versus P, Th, Y, LREE and HREE contents and Zr/Hf ratios. The field enclosed by the *dotted line* represents the composition of pre-Variscan inherited cores. *Symbols* as in legend of Fig. 3

concordia age of 300.5 ± 0.55 Ma (Fig. 7a; MSWD = 0.0065), which we consider the most accurate estimate for the age of intrusion.

Navas del Marqués granite

Sample M9 provided 19 crystallisation ages from a variety of zircon domains: rims with oscillatory zoning and variable CL response and cores with oscillatory or convoluted zoning. Three zircon grains have pre-Variscan ages. One Upper Neoproterozoic age of 564 ± 6 Ma was obtained for an irregular homogeneous dark mineral domain (5.2) located within an Ordovician zircon core (5.1) (Fig. 2e), similarly to what was observed in the Villacastin granite (sample Y24). The other 3 pre-Variscan ages are Ordovician (Table 2; spots 3.1, 5.1 and 20.1) and have been obtained from anhedral to subhedral cores showing a variable CL internal structure, and with a surrounding black rim.

The other analyses have error ellipses overlapping the concordia curve (Fig. 6c). Analysis 13.1 with high U contents, which yielded an anomalous high age of 313 ± 4 Ma, 4 data with high common ^{206}Pb (7.1, 10.1, 14.1 and 17.2) and one spot with high degree of discordance (18.1), have been excluded from the age calculation. The remaining 13 analyses display ^{238}U/^{206}Pb ages in the range 306–280 Ma (Fig. 6c). A selection of eight spots allows the calculation of a concordia age of 300.3 ± 2.6 Ma (MSWD = 0.59) (Fig. 6d).

Atalaya real granite

The 18 SHRMP analyses from sample Y78 do not show inherited zircon. Five analyses corresponding to dark rims or inner domains with sector or irregular zoning exhibit high common ^{206}Pb (analyses 5.1, 5.2, 8.1, 11.1 and 14.1). For the estimation of the crystallisation age, we have not considered these latter data, together with analyses

Table 2 Ion microprobe (SHRIMP) and laser ablation ICP-MS U–Pb analytical data for zircons from SCS granitic intrusions

Spot number	Common ^{206}Pb (%)	U (ppm)	Th (ppm)	Th/U	Radiogenic ratios				Age (Ma)		Disc (%)[a]
					$^{207}Pb/^{235}U \pm \sigma$	$^{206}Pb/^{238}U \pm \sigma$	ρ	$^{207}Pb/^{206}Pb \pm \sigma$	$^{206}Pb/^{238}U \pm \sigma$	$^{207}Pb/^{206}Pb \pm \sigma$	
Hoyo de Pinares (M21)—SHRIMP											
1.1	0.03	4,141	367	0.09	0.3727 ± 1.1	0.0517 ± 1.0	0.93	0.0523 ± 0.4	325 ± 3.2	300 ± 9	−8
2.1	0.18	888	189	0.21	0.3370 ± 1.7	0.0472 ± 1.0	0.61	0.0518 ± 1.4	297 ± 3.0	278 ± 31	−7
3.1	0.00	371	194	0.52	0.3434 ± 1.6	0.0479 ± 1.1	0.68	0.0520 ± 1.2	302 ± 3.3	285 ± 27	−6
4.1	0.17	603	119	0.20	0.3382 ± 2.2	0.0472 ± 1.1	0.49	0.0520 ± 1.9	297 ± 3.1	286 ± 44	−4
4.2	0.72	562	236	0.42	0.3540 ± 3.9	0.0482 ± 1.1	0.28	0.0534 ± 3.8	303 ± 3.3	345 ± 85	14
5.1	0.47	439	143	0.33	0.3160 ± 3.2	0.0446 ± 1.1	0.35	0.0515 ± 3.0	281 ± 3.0	263 ± 68	−7
6.1	0.41	166	130	0.79	0.3410 ± 3.5	0.0488 ± 1.2	0.36	0.0507 ± 3.2	307 ± 3.7	227 ± 75	−26
7.1	0.09	761	107	0.14	0.3474 ± 2.0	0.0483 ± 1.1	0.52	0.0522 ± 1.7	304 ± 3.1	295 ± 40	−3
7.2	0.20	151	69	0.45	1.2193 ± 2.1	0.1370 ± 1.2	0.57	0.0646 ± 1.7	828 ± 9.1	760 ± 36	−8
8.1	0.04	1,548	1,067	0.69	0.3501 ± 1.2	0.0486 ± 1.0	0.83	0.0523 ± 0.7	306 ± 3.1	297 ± 16	−3
8.2	0.12	620	182	0.29	0.3417 ± 1.6	0.0477 ± 1.1	0.65	0.0519 ± 1.2	300 ± 3.1	282 ± 28	−6
9.1	0.29	867	150	0.17	0.3410 ± 1.8	0.0477 ± 1.1	0.59	0.0519 ± 1.4	300 ± 3.1	281 ± 33	−6
10.1	1.25	323	25	0.08	0.4590 ± 7.4	0.0589 ± 1.7	0.24	0.0565 ± 7.2	369 ± 6.2	474 ± 158	28
11.1	0.20	243	78	0.32	0.3423 ± 2.7	0.0483 ± 1.2	0.43	0.0514 ± 2.5	304 ± 3.5	260 ± 56	−14
12.1	0.38	755	519	0.69	0.3344 ± 2.1	0.0459 ± 1.1	0.53	0.0528 ± 1.8	289 ± 3.2	322 ± 41	11
12.2	0.42	364	206	0.57	0.3400 ± 3.6	0.0474 ± 1.1	0.31	0.0520 ± 3.4	299 ± 3.3	286 ± 79	−4
13.1	0.58	68	36	0.53	0.8740 ± 4.0	0.1041 ± 1.4	0.36	0.0609 ± 3.7	638 ± 8.8	636 ± 80	0
14.1	0.08	771	390	0.5	0.3378 ± 2.0	0.0468 ± 1.2	0.59	0.0524 ± 1.6	295 ± 3.4	301 ± 37	2
14.2	0.15	624	185	0.30	0.3381 ± 2.1	0.0478 ± 1.1	0.55	0.0513 ± 1.7	301 ± 3.3	254 ± 40	−16
15.1	0.00	182	76	0.42	0.3334 ± 2.9	0.0458 ± 1.5	0.50	0.0528 ± 2.5	288 ± 4.1	322 ± 58	12
16.1	6.30	767	296	0.39	0.2830 ± 13.0	0.0403 ± 1.3	0.10	0.0509 ± 13.0	255 ± 3.2	235 ± 300	−8
17.1	0.24	410	145	0.35	0.3339 ± 2.5	0.0474 ± 1.2	0.48	0.0511 ± 2.2	299 ± 3.4	244 ± 50	−18
18.1	0.11	402	209	0.52	0.8470 ± 1.9	0.1008 ± 1.3	0.69	0.0610 ± 1.4	619 ± 7.7	637 ± 29	3
19.1	0.20	489	242	0.49	0.3282 ± 2.2	0.0448 ± 1.2	0.52	0.0532 ± 1.9	282 ± 3.2	337 ± 43	19
Alpedrete (Y76)—SHRIMP											
1.1	0.08	802	55	0.07	0.3437 ± 1.6	0.0480 ± 1.1	0.68	0.0519 ± 1.1	302 ± 3.1	282 ± 26	−7
1.2	0.00	106	40	0.38	0.3181 ± 2.7	0.0447 ± 1.3	0.49	0.0516 ± 2.4	282 ± 3.7	269 ± 54	−5
2.1	0.00	200	43	0.21	0.3292 ± 2.9	0.0454 ± 2.4	0.83	0.0526 ± 1.7	286 ± 6.8	311 ± 38	8
2.2	0.19	208	47	0.22	0.3309 ± 2.6	0.0465 ± 1.2	0.45	0.0516 ± 2.3	293 ± 3.4	270 ± 54	−8
3.1	0.22	331	62	0.19	0.3225 ± 2.2	0.0458 ± 1.1	0.51	0.0510 ± 1.9	289 ± 3.2	242 ± 43	−16
3.2	0.00	127	46	0.37	0.3241 ± 4.9	0.0443 ± 4.4	0.89	0.0530 ± 2.2	280 ± 12.0	329 ± 50	18
4.1	0.16	983	277	0.28	0.3286 ± 1.5	0.0459 ± 1.0	0.68	0.0520 ± 1.1	289 ± 3.0	284 ± 26	−2
4.2	0.00	275	94	0.34	0.3037 ± 2.7	0.0414 ± 2.3	0.85	0.0533 ± 1.5	261 ± 5.9	340 ± 33	30

Table 2 continued

Spot number	Common ^{206}Pb (%)	U (ppm)	Th (ppm)	Th/U	Radiogenic ratios				Age (Ma)		Disc (%)[a]
					$^{207}Pb/^{235}U \pm \sigma$	$^{206}Pb/^{238}U \pm \sigma$	ρ	$^{207}Pb/^{206}Pb \pm \sigma$	$^{206}Pb/^{238}U \pm \sigma$	$^{20}Pb/^{206}Pb \pm \sigma$	
5.1	0.04	1,009	276	0.27	0.3326 ± 1.4	0.0466 ± 1.0	0.77	0.0518 ± 0.9	293 ± 3.0	277 ± 20	−6
6.1	0.09	780	241	0.31	0.3385 ± 1.6	0.0473 ± 1.1	0.68	0.0519 ± 1.1	298 ± 3.1	282 ± 26	−5
7.1	0.00	496	103	0.21	0.3333 ± 1.6	0.0460 ± 1.1	0.72	0.0526 ± 1.1	290 ± 3.3	310 ± 25	7
7.2	0.13	319	109	0.34	0.3379 ± 2.2	0.0468 ± 1.1	0.51	0.0524 ± 1.9	295 ± 3.3	301 ± 44	2
8.1	0.11	327	69	0.21	0.3411 ± 2.1	0.0470 ± 1.1	0.53	0.0527 ± 1.8	296 ± 3.3	316 ± 41	7
9.1	0.14	249	57	0.23	0.3374 ± 2.4	0.0471 ± 1.2	0.49	0.0519 ± 2.0	297 ± 3.4	283 ± 47	−5
10.1	0.64	74	78	1.05	0.3124 ± 7.0	0.0449 ± 1.7	0.25	0.0505 ± 6.8	283 ± 4.8	218 ± 157	−23
11.1	0.00	143	58	0.41	0.3161 ± 3.6	0.0434 ± 1.6	0.45	0.0529 ± 3.2	274 ± 4.3	323 ± 73	18
12.1	0.37	976	69	0.07	0.3320 ± 1.8	0.0463 ± 1.1	0.60	0.0520 ± 1.4	292 ± 3.0	287 ± 32	−1
13.1	0.00	278	99	0.36	0.3426 ± 1.8	0.0477 ± 1.2	0.65	0.0521 ± 1.4	300 ± 3.4	290 ± 31	−4
14.1	0.18	527	220	0.42	0.3113 ± 2.2	0.0435 ± 1.5	0.68	0.0519 ± 1.6	275 ± 4.0	280 ± 36	2
15.1	0.45	82	26	0.32	0.3071 ± 5.3	0.0454 ± 1.4	0.27	0.0491 ± 5.1	286 ± 4.0	153 ± 119	−46
16.1	0.34	201	207	1.03	0.3270 ± 4.1	0.0472 ± 1.2	0.30	0.0502 ± 3.9	297 ± 3.5	205 ± 90	−31
17.1	0.18	270	43	0.16	0.7779 ± 1.9	0.0962 ± 1.2	0.64	0.0587 ± 1.5	592 ± 7.0	555 ± 33	−6
18.1	0.31	211	55	0.26	0.3240 ± 3.8	0.0462 ± 1.2	0.32	0.0509 ± 3.6	291 ± 3.4	236 ± 84	−19
19.1	2.21	778	287	0.37	0.1733 ± 5.3	0.0249 ± 1.2	0.23	0.0504 ± 5.1	159 ± 1.9	214 ± 119	35
Alpedrete (Y76)—LA-ICP-MS											
L1	0.00	585	218	0.37	0.2926 ± 3.0	0.0403 ± 1.8	0.32	0.0528 ± 3.0	254 ± 4	319 ± 70	21
L2	0.00	1,614	635	0.39	0.3478 ± 1.6	0.0478 ± 1.4	0.59	0.0528 ± 1.4	301 ± 4	318 ± 32	6
L3	0.00	589	479	0.81	0.3480 ± 2.3	0.0479 ± 1.6	0.42	0.0528 ± 2.2	301 ± 5	319 ± 51	6
L4	0.00	559	354	0.63	0.3541 ± 1.9	0.0482 ± 1.4	0.48	0.0533 ± 1.7	304 ± 4	341 ± 40	11
L5	0.00	1,333	787	0.59	0.3586 ± 2.1	0.0480 ± 1.5	0.45	0.0542 ± 2.0	302 ± 4	381 ± 45	21
L6	3.32	677	741	1.09	0.3508 ± 2.0	0.0467 ± 1.4	0.44	0.0545 ± 1.9	294 ± 4	391 ± 43	25
L7	0.00	912	350	0.38	0.7719 ± 1.4	0.0943 ± 1.3	0.57	0.0594 ± 1.2	581 ± 7	581 ± 27	0
L8	0.00	638	238	0.37	0.3499 ± 2.4	0.0472 ± 1.6	0.39	0.0539 ± 2.3	297 ± 5	365 ± 54	19
L9	0.00	297	125	0.42	0.3239 ± 2.4	0.0458 ± 1.5	0.39	0.0514 ± 2.3	288 ± 4	257 ± 53	−13
L10	0.00	274	66	0.24	0.3611 ± 1.8	0.0490 ± 1.3	0.46	0.0535 ± 1.6	308 ± 4	348 ± 38	12
L11	0.00	370	148	0.40	0.3661 ± 5.2	0.0466 ± 2.3	0.16	0.0571 ± 5.4	294 ± 7	494 ± 121	42
L12	0.00	644	232	0.36	0.3361 ± 2.4	0.0473 ± 1.6	0.39	0.0515 ± 2.3	298 ± 5	265 ± 54	−13
Villacastín (Y24)—SHRIMP											
1.1	2.17	1,871	495	0.26	0.3373 ± 4.8	0.0464 ± 1.1	0.22	0.0528 ± 4.6	292 ± 3.0	319 ± 106	8
2.1	0.79	817	40	0.05	0.5976 ± 2.1	0.0771 ± 1.0	0.51	0.0562 ± 1.8	479 ± 4.8	462 ± 39	−4
3.1	8.60	1,716	479	0.28	0.3458 ± 10.9	0.0445 ± 1.2	0.11	0.0563 ± 10.8	281 ± 3.4	465 ± 239	40
4.1	0.15	1,130	332	0.29	0.3364 ± 1.5	0.0468 ± 1.0	0.70	0.0521 ± 1.1	295 ± 3.0	290 ± 24	−2

Table 2 continued

Spot number	Common ^{206}Pb (%)	U (ppm)	Th (ppm)	Th/U	Radiogenic ratios				Age (Ma)		Disc (%)[a]
					^{207}Pb/^{235}U ± σ	^{206}Pb/^{238}U ± σ	ρ	^{207}Pb/^{206}Pb ± σ	^{206}Pb/^{238}U ± σ	^{20}Pb/^{206}Pb ± σ	
5.1	0.03	1,005	243	0.24	0.3382 ± 1.4	0.0468 ± 1.1	0.76	0.0524 ± 0.9	295 ± 3.1	305 ± 21	3
5.2	4.23	288	124	0.43	0.3653 ± 18.0	0.0482 ± 2.2	0.12	0.0550 ± 17.9	303 ± 6.5	412 ± 400	26
6.1	29.55	92	30	0.33	0.3583 ± 58.4	0.0432 ± 3.8	0.06	0.0601 ± 58.3	273 ± 10.1	607 ± 1260	55
7.1	1.16	1,204	340	0.28	0.3450 ± 3.2	0.0477 ± 1.0	0.33	0.0524 ± 3.0	300 ± 3.1	305 ± 68	1
7.2	3.47	709	169	0.24	0.3342 ± 8.1	0.0460 ± 1.2	0.14	0.0527 ± 8.0	290 ± 3.3	316 ± 181	8
8.1	5.85	178	69	0.39	0.3895 ± 11.5	0.0449 ± 1.5	0.13	0.0629 ± 11.4	283 ± 4.1	703 ± 244	60
9.1	0.65	1,101	335	0.30	0.3349 ± 2.2	0.0465 ± 1.0	0.48	0.0522 ± 1.9	293 ± 3.0	296 ± 44	1
10.1	1.00	996	241	0.24	0.3465 ± 2.5	0.0471 ± 1.1	0.44	0.0534 ± 2.2	297 ± 3.1	345 ± 51	14
11.1	15.44	905	214	0.24	0.2977 ± 24.5	0.0432 ± 1.7	0.07	0.0499 ± 24.4	273 ± 4.5	193 ± 568	−42
12.1	18.13	983	247	0.25	0.3197 ± 29.8	0.0444 ± 2.2	0.07	0.0522 ± 29.7	280 ± 5.9	293 ± 679	4
13.1	0.00	271	91	0.34	0.3324 ± 1.9	0.0462 ± 1.1	0.59	0.0522 ± 1.6	291 ± 3.3	293 ± 36	1
13.2	0.08	2037	461	0.23	0.3418 ± 1.3	0.0474 ± 1.0	0.79	0.0523 ± 0.8	298 ± 3.0	300 ± 18	0
14.1	12.65	1,115	298	0.27	0.3482 ± 14.6	0.0447 ± 1.4	0.10	0.0565 ± 14.5	282 ± 3.8	472 ± 321	40
15.1	0.07	1,305	241	0.18	0.3438 ± 1.4	0.0476 ± 1.1	0.82	0.0523 ± 0.8	300 ± 3.3	300 ± 18	0
16.1	0.16	455	37	0.08	0.5754 ± 1.6	0.0743 ± 1.1	0.66	0.0562 ± 1.2	462 ± 4.8	459 ± 27	−1
17.1	4.50	942	274	0.29	0.3509 ± 12.0	0.0452 ± 1.3	0.11	0.0563 ± 11.9	285 ± 3.5	465 ± 263	39
18.1	8.00	1,915	475	0.25	0.3285 ± 15.2	0.0455 ± 1.3	0.09	0.0523 ± 15.1	287 ± 3.7	300 ± 344	5
19.1	2.33	952	230	0.24	0.3277 ± 5.2	0.0449 ± 1.1	0.21	0.0529 ± 5.1	283 ± 3.0	326 ± 116	13
20.1	0.05	271	10	0.04	0.5742 ± 1.7	0.0746 ± 1.2	0.69	0.0558 ± 1.2	464 ± 5.2	445 ± 27	−4
20.2	0.01	377	215	0.57	5.5240 ± 2.4	0.3339 ± 2.3	0.96	0.1200 ± 0.7	1857 ± 37.4	1956 ± 12	5
21.1	4.74	215	82	0.38	0.3075 ± 11.0	0.0430 ± 1.5	0.13	0.0519 ± 10.9	271 ± 3.9	280 ± 249	3
22.1	0.04	1,804	251	0.14	0.3289 ± 1.3	0.0458 ± 1.0	0.80	0.0521 ± 0.8	289 ± 2.9	289 ± 17	0
Atalaya Real (Y78)—SHRIMP											
1.1	0.01	6,139	2,802	0.46	0.3624 ± 1.1	0.0501 ± 1.0	0.94	0.0524 ± 0.4	315 ± 3.1	305 ± 8	−3
2.1	0.54	575	159	0.28	0.3161 ± 2.8	0.0427 ± 1.1	0.38	0.0537 ± 2.6	270 ± 2.8	357 ± 59	24
2.2	0.09	1,222	245	0.20	0.3366 ± 1.4	0.0468 ± 1.1	0.73	0.0521 ± 1.0	295 ± 3.0	291 ± 22	−1
3.1	0.24	210	76	0.36	0.3427 ± 2.7	0.0485 ± 1.3	0.49	0.0512 ± 2.4	305 ± 4.0	251 ± 55	−22
4.1	0.12	280	112	0.40	0.3456 ± 1.9	0.0479 ± 1.1	0.57	0.0523 ± 1.6	302 ± 3.3	298 ± 36	−1
5.1	5.47	866	270	0.31	0.3115 ± 7.3	0.0433 ± 1.1	0.16	0.0522 ± 7.2	273 ± 3.0	295 ± 164	7
5.2	11.42	349	188	0.54	0.2047 ± 18.7	0.0284 ± 1.6	0.09	0.0524 ± 18.6	180 ± 2.8	301 ± 424	40
6.1	0.00	449	153	0.34	0.3439 ± 1.5	0.0471 ± 1.1	0.71	0.0530 ± 1.1	297 ± 3.2	327 ± 25	9
6.2	0.19	1,048	637	0.61	0.3415 ± 1.6	0.0479 ± 1.0	0.65	0.0517 ± 1.2	302 ± 3.1	271 ± 28	−11
7.1	0.58	574	199	0.35	0.3411 ± 3.0	0.0470 ± 1.1	0.36	0.0527 ± 2.8	296 ± 3.1	314 ± 64	6
7.2	0.23	5,022	390	0.08	0.3450 ± 1.2	0.0477 ± 1.0	0.88	0.0525 ± 0.6	300 ± 3.0	305 ± 13	2

Table 2 continued

Spot number	Common ^{206}Pb (%)	U (ppm)	Th (ppm)	Th/U	Radiogenic ratios				Age (Ma)		Disc (%)[a]
					$^{207}Pb/^{235}U \pm \sigma$	$^{206}Pb/^{238}U \pm \sigma$	ρ	$^{207}Pb/^{206}Pb \pm \sigma$	$^{206}Pb/^{238}U \pm \sigma$	$^{207}Pb/^{206}Pb \pm \sigma$	
8.1	4.76	322	112	0.35	0.2594 ± 9.4	0.0368 ± 1.3	0.13	0.0511 ± 9.3	233 ± 2.9	245 ± 214	5
9.1	0.22	1,406	289	0.21	0.3532 ± 1.6	0.0486 ± 1.0	0.66	0.0527 ± 1.2	306 ± 3.1	315 ± 27	3
10.1	0.21	271	65	0.24	0.3446 ± 2.7	0.0485 ± 1.2	0.42	0.0515 ± 2.5	305 ± 3.4	265 ± 57	−15
11.1	9.53	298	124	0.41	0.3173 ± 22.1	0.0449 ± 1.6	0.07	0.0513 ± 22.0	283 ± 4.4	254 ± 506	−11
12.1	0.00	263	122	0.46	0.3423 ± 2.2	0.0428 ± 1.2	0.52	0.0580 ± 1.9	270 ± 3.1	531 ± 42	49
13.1	0.67	149	109	0.73	0.3314 ± 7.0	0.0490 ± 1.3	0.19	0.0490 ± 6.9	308 ± 3.9	149 ± 161	−106
14.1	7.45	227	89	0.39	0.3392 ± 16.1	0.0431 ± 1.9	0.12	0.0571 ± 16.0	272 ± 5.1	494 ± 352	45
Navas del Marqués (M9)—SHRIMP											
1.1	0.00	219	71	0.32	0.3340 ± 2.1	0.0459 ± 1.3	0.63	0.0527 ± 1.6	289 ± 3.7	318 ± 37	9
2.1	0.38	280	102	0.36	0.3499 ± 4.1	0.0486 ± 1.3	0.33	0.0522 ± 3.9	306 ± 4.0	296 ± 88	−3
3.1	0.00	204	97	0.47	0.5947 ± 1.8	0.0747 ± 1.3	0.71	0.0577 ± 1.3	465 ± 5.8	519 ± 28	10
4.1	1.26	133	64	0.48	0.3254 ± 7.9	0.0445 ± 1.5	0.19	0.0530 ± 7.7	281 ± 4.1	330 ± 176	15
5.1	0.25	306	23	0.08	0.5749 ± 2.7	0.0751 ± 1.3	0.48	0.0555 ± 2.3	467 ± 5.8	433 ± 52	−8
5.2	0.59	2537	861	0.34	0.7430 ± 1.5	0.0915 ± 1.2	0.80	0.0589 ± 0.9	564 ± 6.4	564 ± 19	0
6.1	0.30	232	79	0.34	0.3353 ± 3.3	0.0466 ± 1.3	0.40	0.0521 ± 3.1	294 ± 3.8	291 ± 70	−1
7.1	6.08	667	386	0.58	0.3547 ± 16.8	0.0483 ± 1.5	0.09	0.0532 ± 16.7	304 ± 4.5	338 ± 379	10
7.2	0.25	272	82	0.30	0.3430 ± 3.2	0.0479 ± 1.3	0.41	0.0519 ± 2.9	302 ± 3.9	282 ± 67	−7
8.1	0.17	1,464	438	0.30	0.3437 ± 1.6	0.0478 ± 1.2	0.75	0.0522 ± 1.1	301 ± 3.5	293 ± 24	−3
9.1	0.90	1,203	267	0.22	0.3349 ± 2.4	0.0467 ± 1.2	0.51	0.0520 ± 2.0	294 ± 3.5	285 ± 47	−3
10.1	2.86	937	229	0.24	0.3311 ± 7.3	0.0470 ± 1.3	0.17	0.0511 ± 7.2	296 ± 3.6	244 ± 167	−21
11.1	0.19	2035	734	0.36	0.3425 ± 1.6	0.0479 ± 1.2	0.75	0.0519 ± 1.1	302 ± 3.5	279 ± 24	−8
12.1	0.38	405	169	0.42	0.3407 ± 3.9	0.0473 ± 1.3	0.33	0.0522 ± 3.7	298 ± 3.7	296 ± 84	−1
13.1	0.33	3227	1049	0.33	0.3615 ± 1.6	0.0498 ± 1.2	0.76	0.0527 ± 1.1	313 ± 3.7	315 ± 24	1
14.1	5.00	371	122	0.33	0.3327 ± 17.8	0.0459 ± 1.4	0.08	0.0525 ± 17.7	290 ± 4.0	308 ± 404	6
15.1	1.14	473	277	0.59	0.3383 ± 4.4	0.0472 ± 1.3	0.29	0.0520 ± 4.2	297 ± 3.7	287 ± 97	−4
16.1	0.61	773	151	0.20	0.3335 ± 2.3	0.0463 ± 1.2	0.52	0.0522 ± 2.0	292 ± 3.5	296 ± 45	1
17.1	0.09	513	257	0.50	0.3495 ± 2.0	0.0482 ± 1.2	0.62	0.0526 ± 1.6	303 ± 3.7	313 ± 36	3
17.2	5.93	994	876	0.88	0.3272 ± 8.5	0.0455 ± 1.3	0.16	0.0521 ± 8.4	287 ± 3.7	292 ± 192	2
18.1	0.43	185	102	0.56	0.3389 ± 3.8	0.0483 ± 1.4	0.36	0.0509 ± 3.6	304 ± 4.1	235 ± 82	−30
19.1	0.76	493	156	0.32	0.3349 ± 2.9	0.0470 ± 1.3	0.43	0.0517 ± 2.7	296 ± 3.6	271 ± 61	−9
20.1	0.00	354	26	0.07	0.6113 ± 1.6	0.0769 ± 1.3	0.78	0.0577 ± 1.0	478 ± 5.8	517 ± 22	8

Uncertainties given at the one sigma level. Common Pb corrected using measured ^{204}Pb. ρ error correlation between $^{206}Pb/^{238}U$ and $^{207}Pb/^{235}U$ ratios

[a] *Disc* U–Pb discordance, difference between the ^{204}Pb-corrected $^{206}Pb/^{238}U$ and $^{207}Pb/^{206}Pb$ ages

Table 3 CA-ID-TIMS U–Pb analytical data for zircons from SCS granitic intrusions

Fraction	Weight (mg)	Concentration		Measured[a]			Corrected atomic ratios				Age (Ma)		
		U (ppm)	Pb* (ppm)	Pb_c (pg)	$^{206}Pb/^{204}Pb^*$	$^{208}Pb/^{206}Pb^*$	$^{206}Pb/^{238}U \pm \sigma$	$^{207}Pb/^{235}U \pm \sigma$	ρ	$^{207}Pb/^{206}Pb \pm \sigma$	$^{206}Pb/^{238}U$	$^{207}Pb/^{235}U$	$^{207}Pb/^{206}Pb$
Villacastín (Y24)													
Z1													
10 Xtls. CA	0.04	328	17.7	61.0	493	0.1260	0.04769 ± 0.42	0.34418 ± 2.42	0.18	0.05234 ± 2.38	300.3	300.3	300.4
Z2													
5 Xtls. CA	0.02	102	5.18	9.5	361	0.1015	0.04784 ± 0.32	0.34531 ± 0.92	0.48	0.05235 ± 0.82	301.2	301.2	300.9
Z3													
15 SM xtls. CA	0.07	303	15.3	41.0	1,022	0.1126	0.04773 ± 0.22	0.34436 ± 1.02	0.39	0.05233 ± 0.95	300.5	300.5	299.9
Z4													
10 SM xtls. CA	0.03	170.84	8.7	22	540	0.1188	0.0475 ± 0.43	0.34270 ± 0.77	0.63	0.052326 ± 0.60	299.2	299.2	299.7
Atalaya Real (Y78)													
Z1													
3 xtls. CA	0.04	168	9.9	49.9	311	0.1340	0.04857 ± 0.17	0.35159 ± 0.49	0.46	0.05250 ± 0.44	305.7	305.9	307.2
Z2													
15 SM xtls. CA	0.05	288	14.0	14.6	2,147	0.1035	0.04855 ± 0.34	0.35124 ± 0.44	0.80	0.05247 ± 0.27	305.6	305.7	306.0
Z3													
6 Xtls. CA	0.03	210	10.8	15.3	1,015	0.1185	0.04862 ± 0.20	0.35216 ± 0.30	0.69	0.05253 ± 0.22	306.0	306.3	308.7
Z4													
14 Xtls. CA	0.04	260	14.4	49.5	454	0.1280	0.04838 ± 0.24	0.34991 ± 0.62	0.41	0.05246 ± 0.57	304.6	304.7	305.3
Z5													
6 Xtls. CA	0.05	245	12.5	20.3	1,341	0.1240	0.04860 ± 0.29	0.35151 ± 1.50	0.44	0.05245 ± 1.40	305.9	305.9	305.2

Xtls euhedral zircon prisms, 1:3–1:5 width/length ratio. *SM* small (<100 mm), *CA* chemically abraded (Mattison 2005). Weight estimated before CA. Pb (pg): total Pb blank

[a] Measured ratio corrected for blank and fractionation. Atomic ratios corrected for fractionation (0.11 ± 0.02% AMU Pb; 0.10 ± 0.02% AMU U), spike (^{208}Pb–^{235}U) laboratory blanks (6 pg Pb; 0.1 pg U) and initial common Pb after Stacey and Kramers (1975). Errors are at the 2-sigma level. Data reduced with PbMacDat (Isachsen et al. http://www.earth-time.org). Pb^* radiogenic lead, Pb_c total common lead. ρ error correlation between $^{206}Pb/^{238}U$ and $^{207}Pb/^{235}U$ ratios

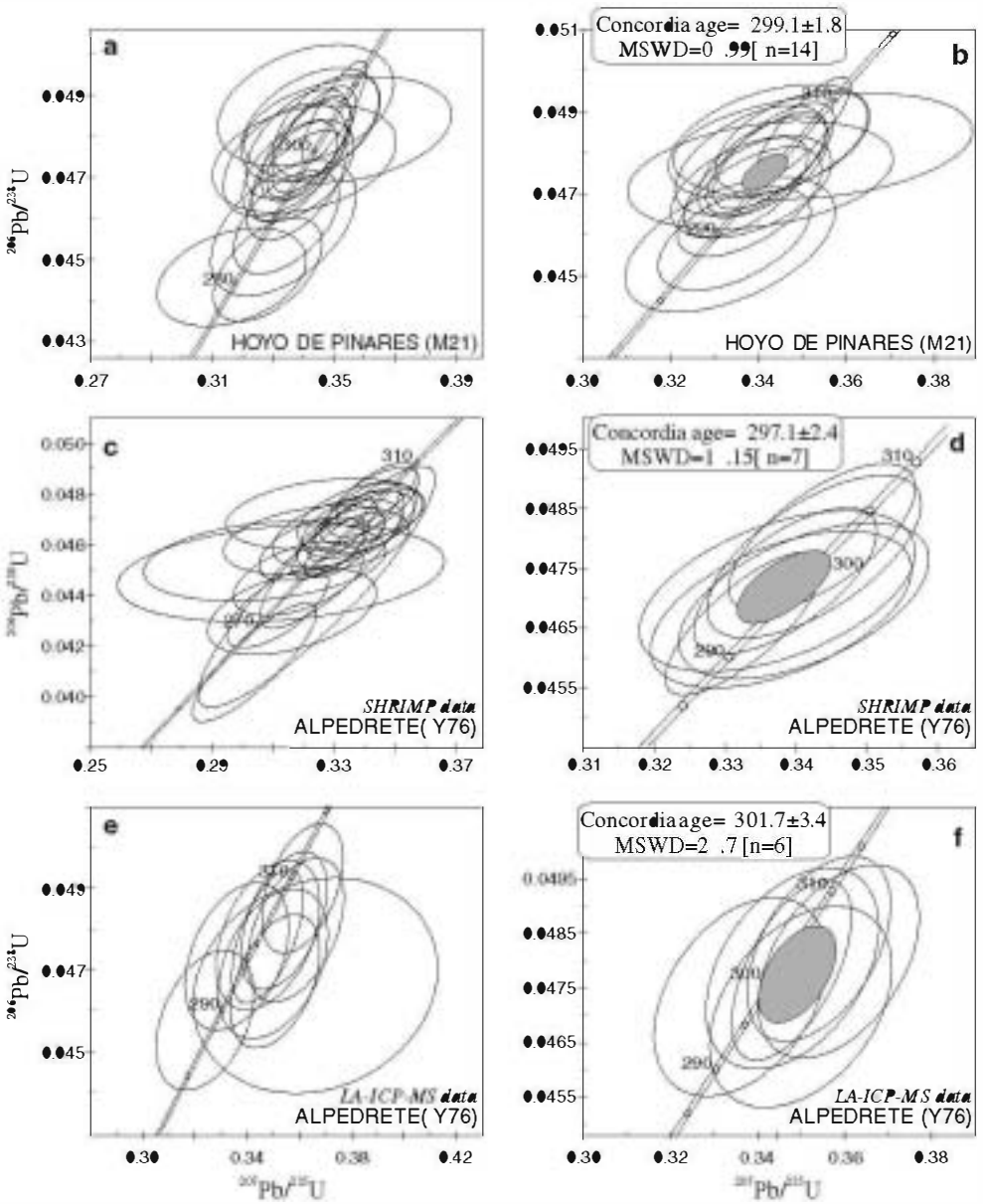

Fig. 5 **a**, **c**, **e** Concordia diagrams showing the SHRIMP and LA-ICP-MS U–Pb data for Variscan zircons from samples M21 and Y76, except a few analyses with exceedingly high or low concordia ages. Concordia age plots (**b**, **d**, **f**) in the *right* consider a restricted group of selected spots. *Error ellipses* are given at the 2σ level

displaying high U and four spots with high %discordance (2.1, 3.1, 12.1 and 13.1). The rest of data (7 analyses) represent ages from 295 to 306 Ma (Fig. 6e). Five of these data were selected and provided a concordia age of 302.3 ± 2.9 Ma (MSWD = 0.002) (Fig. 6f). This age is consistent with the probability density function, which shows a maximum of the bin distribution towards 302–304 Ma (Fig. 6g).

The five fractions analysed by CA-ID-TIMS form a cluster on concordia between 304 and 307 Ma and provide a concordia age of 305.68 ± 0.41 Ma (Fig. 7b; MSWD = 0.33), which is considered the most accurate estimate for the age of intrusion.

Discussion

Zircon composition and Ti-in-zircon thermometry

The steep patterns from MREE to HREE normalised values shown by zircons from the sampled SCS granites (Fig. 3a, b), in conjunction with dominant oscillatory zoning,

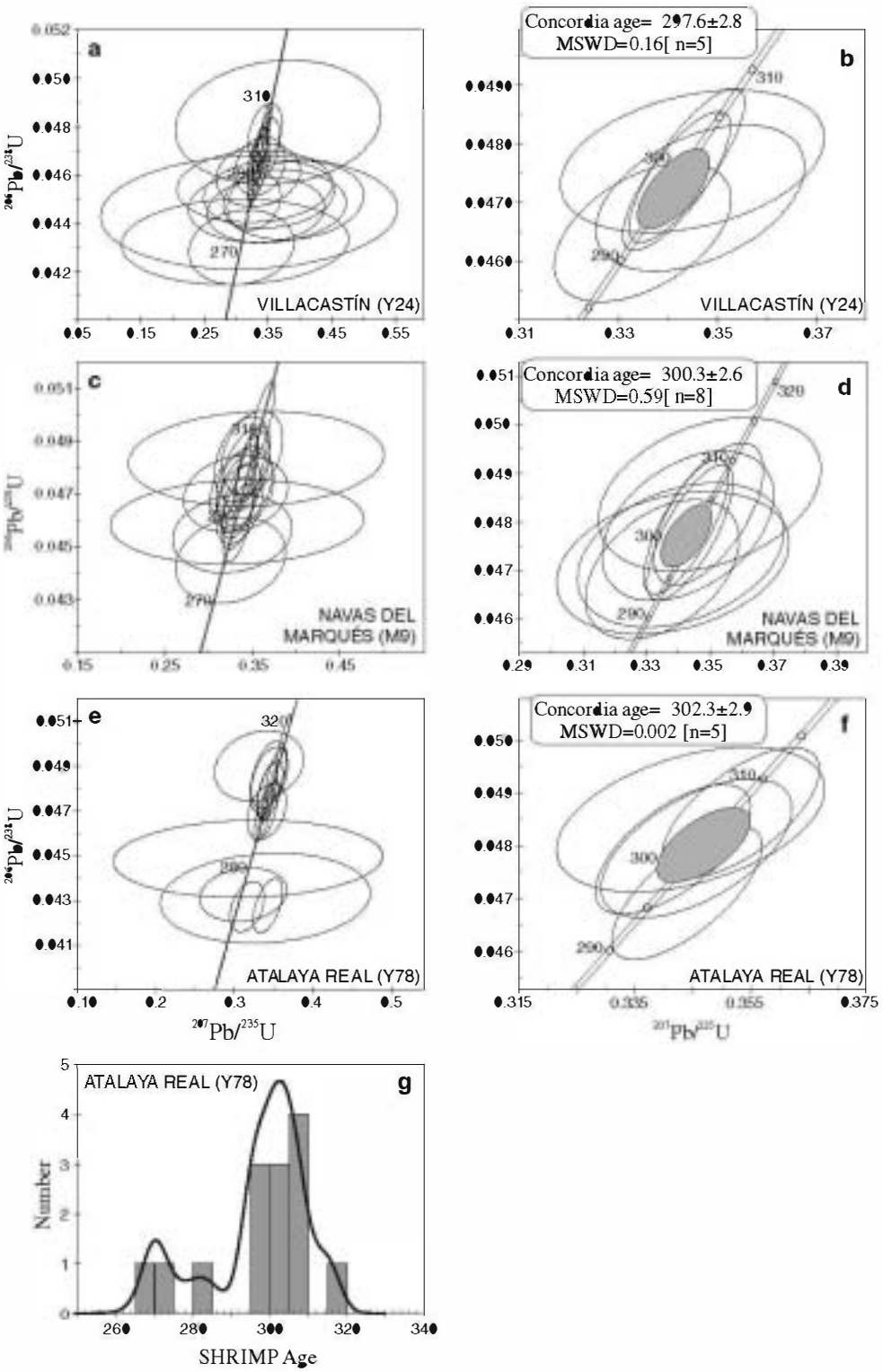

Fig. 6 **a**, **c**, **e** Concordia diagrams showing the SHRIMP U–Pb data for Variscan zircons from samples Y24, Y78 and M9, except a few analyses with exceedingly low concordia ages. Concordia age plots (**b**, **d**, **f**) in the *right* consider a restricted group of selected spots. **g** Probability density plot made for sample Y78 (2σ *errors* used for calculation). *Error ellipses* are given at the 2σ level

evidence the igneous origin of Variscan zircons. The anomalous high LREE contents in 3 spots: Y24-02, Y24-09 and M9-11 (Fig. 3a), which have been analysed in dark bands from oscillatory-zoned domains, are likely associated with secondary modifications at late magmatic stages. Preferential concentration of LREE, U, Th and other large cations has been described in zircons with similar CL textures and explained as alteration phenomena during magma cooling (Pidgeon et al. 1998).

The trace element variability of Variscan zircons (Figs. 3, 4) suggests the possibility of crystallisation from several magmas, an evolving melt or a combination of both

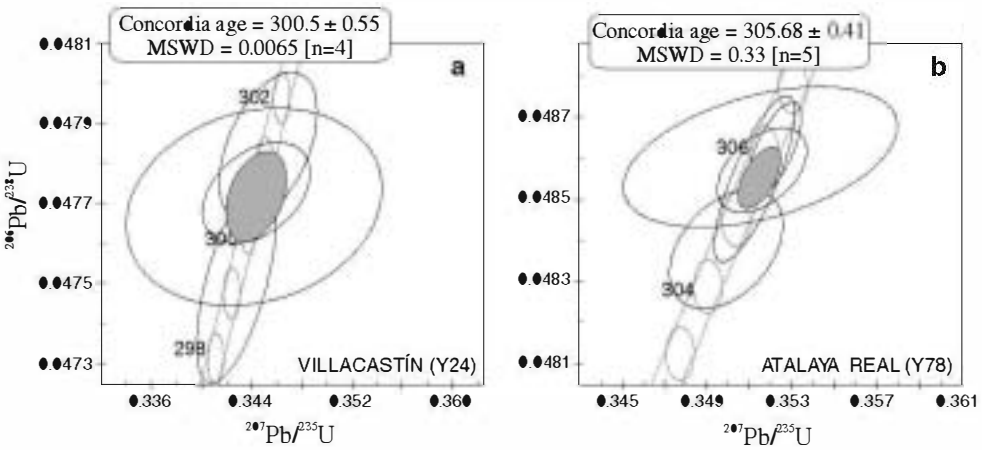

Fig. 7 Concordia diagrams showing the TIMS U–Pb data for Variscan zircons from samples Y24 **a** and Y78 **b**. *Error ellipses* are given at the 2σ level

factors. Significant intra-mineral chemical heterogeneity between sectors separated by resorption surfaces has been described in magmatic zircons and ascribed to Zr undersaturation during recharge with hotter ascending magma (Belousova et al. 2006; Claiborne et al. 2006; Gagnevin et al. 2010). These abrupt changes in trace element concentrations, however, can coexist with a long-term inter-mineral chemical variation related to melt evolution (e.g. Claiborne et al. 2006). Variscan zircons analysed for the present study show textural features in agreement with resorption stages during magma cooling (e.g. Fig. 2c, grain 7; Fig. 2e, grain 18). But the spots selected for laser ablation analysis do not allow the discussion of intra-mineral chemistry and magma mixing processes. Anyway, the trace element contents of SCS zircons are characteristic of granitoid rocks (Nb = 1–17 ppm, Ta = 0.32–12 ppm and Eu/Eu* < 0.3) (Belousova et al. 2002) and exhibit crustal signatures (Zr/Hf = 32–58) (Pupin 2000), so mixing with felsic magmas is preferred rather than implication of mantle-derived melts.

The degree of magma differentiation can correlate positively with the abundance of Hf in igneous zircon (Hoskin and Schaltegger 2003 and references therein). Experiments by Linnen and Keppler (2002) concluded that this effect is related to modifications of the Zr/Hf ratio during crystal fractionation of granitic melts. SCS granite zircons display a positive correlation between Hf and U-Nb (Ta) (Fig. 3b, c), whilst Zr/Hf ratio decreases (Fig. 4). These characteristics are in accordance with a progressive increase in the degree of magma evolution and an incompatible behaviour of U, Nb and Ta with respect to the fractionating mineral assemblage. However, the response shown by other trace elements is fairly variable and dependent on the intrusion considered, pointing to influence of co-precipitating trace element-rich accessory phases. These minerals would withdraw highly incompatible elements and compensate for their enrichment in the melt during differentiation. Common accessory phases in these rocks are REE-rich phosphates (apatite, monazite and xenotime). Their involvement during crystal fractionation can be envisaged in S-type granites zircons [Alpedrete (Y76) and Hoyo de Pinares (M21)] on the basis of the lack of P increase with higher Hf (Fig. 4). These intrusions do not show significant trends for REE, Y and Th, thus supporting that monazite and xenotime are likely the main accessory minerals associated with magma differentiation. On the other hand, P, Y and HREE from Villacastín (Y24) and Atalaya Real (Y78) zircons are positively correlated with Hf (Fig. 4). This characteristic is likely related to the "xenotime" coupled substitution mechanism in zircon (e.g. Hoskin and Schaltegger 2003), which adds to the effect caused by magma evolution. However, LREE contents in these zircons do not correlate significantly with the degree of differentiation (Fig. 4). Fractionation of a LREE-rich silicate, such as allanite, might be responsible for this behaviour. Monazite and allanite are the predominant fractionating LREE-rich minerals in the SCS S- and I-type granitoids, respectively (Villaseca et al. 1998). This agrees well with the proposed implication of these accessory phases during magma fractionation. Moreover, a recent study by Pérez-Soba et al. (2007) has highlighted a similar influence of accessory minerals in the zircon chemistry of several granitic intrusions of eastern SCS (including Alpedrete and Atalaya Real). The fact that Navas del Marqués zircons present a general increase in all trace elements towards higher Hf or U supports that no accessory minerals have significantly modified zircon chemistry during its growth.

The analysed pre-Variscan zircons, irrespective of their crystallisation age, show a trace element composition overlapping that of the Variscan grains (Figs. 3, 4; Table 1). This similarity indicates that the inherited zircons likely originated from a granitic melt, which would be in accordance with the predominance of felsic peraluminous magmatism occurring in the CIZ during Lower Palaeozoic (e.g. Bea et al. 2003; Zeck et al. 2004; Montero et al. 2009).

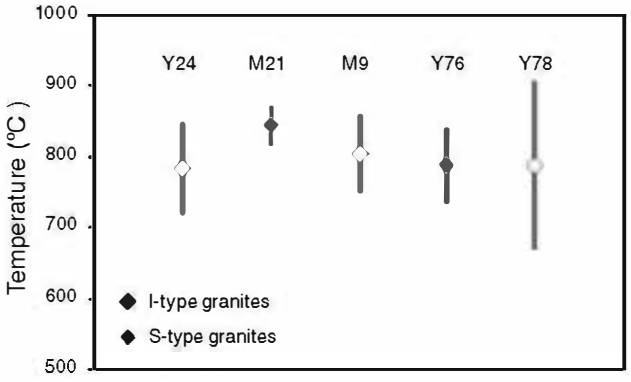

Fig. 8 Mean temperatures of the five S- and I-type granite samples calculated using the recalibrated Ti-in-zircon geothermometer of Ferry and Watson (2007). The *grey bar* represents the *error* associated with each data. Fairly similar high temperatures have been obtained for either S- or I-type granites

We have estimated the temperature of crystallisation of each intrusion on the basis of Ti concentrations using the recalibrated Ti-in-zircon equation of Ferry and Watson (2007). Due to absence of rutile and presence of ilmenite in these granites, we have assumed an $a(TiO_2)$ value of 0.6, typical of silicic melts (Ferry and Watson 2007). The calculated mean temperatures are quite similar in S-type granites: 844°C (Hoyo de Pinares) and 788°C (Alpedrete), and I-type granites: 784°C (Villacastín), 787°C (Atalaya Real) and 804°C (Navas del Marqués) (Fig. 8). Temperature subestimation or overestimation in the order of ~40°C would result from the application of $a(TiO_2) = 1$ or 0.5, respectively. The T range obtained for the SCS granite zircons (784–844°C) represents relatively elevated temperatures in all cases (Fig. 8). These temperatures are equivalent to those proposed for "hot" granites (e.g. Miller et al. 2003) and are indicative of a deep level of melting, likely within the lower crust. The low number of zircon inheritances preserved in the five samples is in agreement with the above high-T data.

Constraints on the protolith nature

Only 14 pre-Variscan ages have been recorded in several zircon cores from 4 of the analysed samples, defining a total age range of c. 369–1,956 Ma (Table 2). Although this dataset is very limited and should be taken with caution, it is interesting to note that two groups of ages might be distinguished: (1) six analyses define a fairly restricted cluster of 462–479 Ma and (2) seven inherited cores recorded ages older than 564 Ma (1,956–564 Ma). The age of 369 Ma (sample M21) from an inherited core with convoluted zoning is younger than any possible source rock in the region (either magmatic or sedimentary), so it is considered to be the result of secondary processes. The

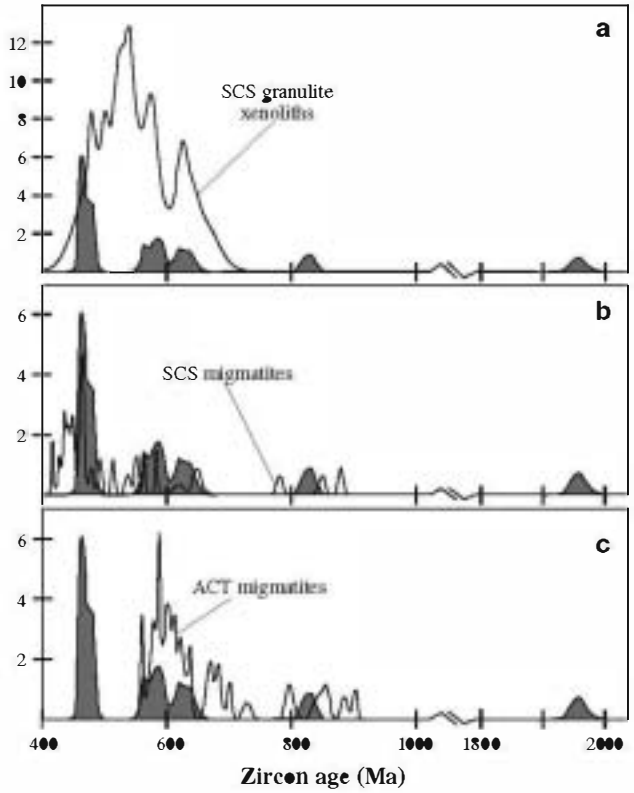

Fig. 9 Relative probability plots of pre-Variscan ages registered in zircons from SCS granitic intrusions (*grey fields*). Similar density curves with U–Pb zircon ages from **a** SCS granulite xenoliths, **b** SCS migmatites derived from metaigneous protoliths (Sotosalbos samples; Castiñeiras et al. 2008) and **c** Anatectic Complex of Toledo (ACT) migmatites derived from metasedimentary protoliths (Castiñeiras et al. 2008), have also been plotted for comparison. See that the inheritances in the SCS granites match better the *curves* of igneous-derived rocks **a** and **b**

density curve that represents these data has been plotted in Fig. 9, in comparison with inherited ages from deep-seated SCS granulite xenoliths and outcropping metamorphic rocks from central Spain.

The six Ordovician ages are all recorded in I-type granites (Villacastín and Navas del Marqués). These two samples also show Neoproterozoic (564 Ma) and lower Proterozoic (1,956 Ma) inheritances, but both data represent texturally discordant cores within Ordovician zircon domains (Fig. 2c, grain 20; Fig. 2e, grain 5). S-type granites (Hoyo de Pinares and Alpedrete) present pre-Variscan cores older than 580 Ma (828–581 Ma). This clear contrast in the age of inheritances suggests that two distinct source rocks were involved in the genesis of the two SCS granitic series. Different sources for SCS S- and I-type granites were not obvious using classical geochemical approaches (Sr, Nd, O, Pb isotopes) (e.g. Villaseca et al. 1998, 2009; Villaseca and Herreros 2000). Thus, the study of zircon inheritances by U–Pb geochronology is a powerful tool in discriminating igneous protoliths.

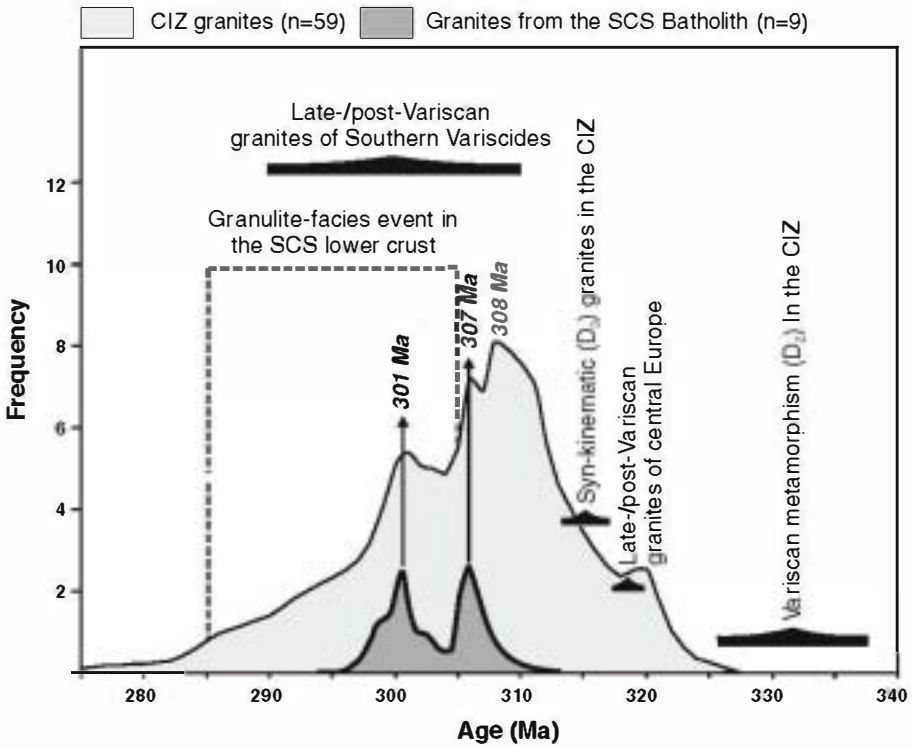

Fig. 10 Relative probability plot showing precise geochronology results for granites from the CIZ (Dias et al. 1998; Fernández-Suárez et al. 2000; Valle Aguado et al. 2005; Zeck et al. 2007b; Antunes et al. 2008; Carracedo et al. 2009; Martins et al. 2009; Neiva et al. 2009; Solá et al. 2009; Díaz-Alvarado et al. 2011; unpublished data) and from the Spanish Central System (Zeck et al. 2007b; Díaz-Alvarado et al. 2011; this study). The timing of several metamorphic and magmatic events in the Iberian Massif or other western Variscides have also been represented for comparison (*horizontal black bands*): the Variscan D2 metamorphic phase in the CIZ (Escuder-Viruete et al. 1998; Valverde-Vaquero 1998), the intrusion of late-/post-kinematic Variscan granites in central Europe (Klein et al. 2008 and references therein), the intrusion of syn-kinematic (D3) granites in the CIZ (e.g. Dias et al. 1998; Valle Aguado et al. 2005), the intrusion of late-/post-kinematic Variscan granites in the southern Variscides (Roberts et al. 2000; Ledru et al. 2001; Cocherie et al. 2005; Fiannacca et al. 2008; Ballèvre et al. 2009; Dallagiovanna et al. 2009) and the granulite-facies metamorphism in the Spanish Central System lower crust (Fernández-Suárez et al. 2006; Órejana et al. 2011)

An important Ordovician magmatic event has been identified in the CIZ. U–Pb zircon dating has yielded crystallisation ages from 496 to 468 Ma (Valverde-Vaquero and Dunning 2000; Zeck et al. 2007a; Montero et al. 2009). Abundant inherited zircons corresponding to similar Ordovician ages (~480–464 Ma) have also been found in Variscan migmatites from the SCS (Castiñeiras et al. 2008) (Fig. 9b). The presence of very similar Ordovician ages in (1) magmatic zircons from metaigneous rocks outcropping in central Spain, (2) pre-Variscan zircon cores from SCS lower crustal granulite xenoliths (490–460 Ma; Fernández-Suárez et al. 2006; Órejana et al. 2011) and (3) inherited grains from SCS I-type granites (Fig. 9) suggests that the source materials of these latter intrusions might be Ordovician plutonic rocks metamorphosed during the Variscan collision at lower crustal levels. The two older zircon grains included in a total of six Ordovician cores must represent inheritances from the orthogneis protolith. The abundance of such zircon inclusions from the source rocks is a main characteristic of the CIZ Ordovician metaigneous rocks (Bea et al. 2007).

The scarce and dispersed pre-Ordovician zircon ages obtained from the SCS S-type granites do not allow a clear interpretation. They mainly spread from 638 to 581 Ma (the only data outside this range is 828 Ma). A Cadomian magmatic event has been identified in central Spain on the basis U–Pb zircon geochronology of outcropping augen gneisses from western SCS (~547–543 Ma; Bea et al. 2003; Zeck et al. 2004). Texturally discordant cores from other CIZ metaigneous rocks reveal abundant zircon populations formed during the Upper Proterozoic-Cambrian (~580–500 and ~650–600 Ma; Bea et al. 2007; Montero et al. 2009; Castiñeiras et al. 2008). However, the nature of the inherited pre-Cambrian ages is controversial, being assigned either to magmatic (e.g. Bea et al. 2007; Montero et al. 2009) or metasedimentary (Zeck et al. 2004, 2007a) protoliths. Our results for the S-type granites closely approximate the above Cadomian ages, but also data from

metasediments outcropping in central Spain (Fig. 9c). A recent paper by Fernández-Suárez et al. (2011) highlights the overwhelming predominance of inherited ages younger than ~650 Ma in many granitic intrusions from the Iberian Variscan Belt. These authors conclude that these felsic Variscan granites are mainly related to Cambro-Ordovician metaigneous protoliths and that influence of sedimentary components might derive from contamination. Our data on zircons from SCS granites are in accordance with this hypothesis, and the presence of ages older than 650 Ma allows the involvement of metasediments in the orthogneiss source region during the Cambro-Ordovician magmatic event. However, we think that other kind of data (such as Lu–Hf isotopes) would be necessary for a deeper discussion on the nature of the granites protolith.

Constraints on the age of intrusion of the SCS batholith

The age spread shown by zircon analyses is too extensive to represent the crystallisation of a magmatic system. We think that this age scattering is likely induced by Pb-loss. Accordingly, we have considered the highest apparent ages from each sample as the best approximation to the age of crystallisation. This is supported by the probability density plot made for sample Y78 (Atalaya Real), which displays a maximum towards the oldest values (between 302 and 304 Ma; Fig. 6g), very similar to the average age obtained by CA-ID-TIMS. Thus, the SHRIMP concordia ages (2σ errors) have been calculated excluding analyses more likely influenced by Pb-loss (Figs. 5, 6).

The initial works focused on the geochronology of CIZ magmatic intrusions have usually applied the K–Ar or Rb–Sr isochron methods (either on whole-rock or mineral separates), resulting in poorly reliable data spreading in a wide time span (e.g. Serrano Pinto et al. 1987, and references therein). A general range of 327–284 Ma was proposed for the intrusion of the SCS felsic batholith (e.g. Villaseca et al. 1998; Bea et al. 1999). Recently, more attempts have been made to better constrain the intrusion of the granitic plutons of western and central Iberian Peninsula, and most of them have focused on U–Th–Pb zircon and monazite data via TIMS, ion microprobe, laser ablation ICP-MS or electron microprobe (Dias et al. 1998; Fernández-Suárez et al. 2000; Bea et al. 2006; Zeck et al. 2007b; Antunes et al. 2008; Neiva et al. 2009; Solá et al. 2009). According to these data, most of the felsic magmatism in the CIZ is sin- or post-tectonic with respect to the last ductile deformation phase (D_3) (Dias et al. 1998; Fernández-Suárez et al. 2000; Valle Aguado et al. 2005), implying intrusion after approximately 320 Ma. Older sin-D_2 intrusions are scarce and have been recognised in the West Asturian Leonese Zone (Fernández-suárez et al. 2000). This age distribution is apparent from the probability density curve made for available precise U–Pb ages determined in granitoids from the CIZ (Fig. 10; see references in figure caption). In this latter diagram, there is a small peak at 320 Ma, which corresponds mainly to syn-D_3 leucogranites from north-western Iberia, but the bulk of data yield larger peaks at 308–306 Ma and 301 Ma. These younger ages have been obtained for late- or post-tectonic granites in the whole CIZ.

The only accurate data on Variscan felsic intrusions from central Spain are those provided by Zeck et al. (2007b) and Díaz-Alvarado et al. (2011) for the Spanish Central System (Fig. 1a), which present four granitic bodies from western SCS crystallised in the range of 308–303 Ma. On the other hand, the detailed studies of several anatectic areas made by Bea et al. (2006) and Castiñeiras et al. (2008), have established the age of the migmatisation in mid-crustal levels from central Spain in the broad range of 330–317 Ma. Taking into account the scarcity of precise data in central Spain, the geochronology of the five granites from eastern SCS studied here represents an important contribution to constrain the time of intrusion of this batholith. Their age of crystallisation (305–298 Ma) partially overlap the results of Zeck et al. (2007b) and Díaz-Alvarado et al. (2011) and allows a classification as post-D_3 intrusions. However, it should be noted that most of our data (4 of the 5 analysed plutons) are younger than 302 Ma (the exception is Atalaya Real with 305.7 Ma), whereas the available data from western SCS are mostly older than 306 Ma. Accordingly, it is possible to distinguish two magmatic pulses (one about 301 Ma and other about 306 Ma), which are clearly related to the main peaks drawn by the whole dataset for CIZ granites (Fig. 10).

These data seem to favour a younger time of emplacement for plutons from the eastern SCS when compared with granites from the western SCS. Moreover, they suggest that the SCS Variscan magmatism is among the youngest igneous manifestations in the CIZ, intruding after the peak of maximum magmatic activity (latter than 309 Ma). This new age dating represents a shorter time period when compared with the previous geochronology on the same granites (Villaseca et al. 1998, and references therein). This is also supported by precise dating of the contemporary basic magmatism: small gabbroic bodies from the SCS yielded ages ranging from 312 to 300 Ma (Montero et al. 2004; Bea et al. 2006; Zeck et al. 2007b; Villaseca et al. 2011).

The origin of the SCS Batholith has been related to melting of the lower crust on the basis of whole-rock geochemistry of deep-seated granulitic xenoliths (Villaseca et al. 1999). Recent studies based on U–Pb zircon ages in these SCS granulites reinforces this conclusion, showing an abundant population of metamorphic zircons formed in the

range 320–275 Ma (Fernández-Suárez et al. 2006; Orejana et al. 2011). Although these values show a relative dispersion, there is an overwhelming presence of zircons with ages in the more restricted time span of 305–285 Ma, which perfectly match the age of crystallisation of the five analysed granites (Fig. 10). Fernández-Suárez et al. (2006) suggested that two magmatic pulses might be envisaged in the CIZ during the Variscan orogeny: 300–295 and 280–288 Ma, due to a similar pattern found in granites from northwest Spain (Fernández-Suárez et al. 2000). Nevertheless, we think that this hypothesis could not be suitable for central Spain and should be confirmed by further geochronological work, because no evidence of Variscan felsic intrusions younger than 290 Ma has been found in the Spanish Central System.

The elevated temperatures (784–844°C) estimated for the five sampled granites (Fig. 8) are in agreement with the possibility of melting at deep crustal levels. An important thermal input from the mantle might have played a key role in heating the base of the crust, as proposed by Zeck et al. (2007b). Taking into account that both SCS basic and silicic magmas represent a coetaneous post-collisional late-orogenic event, melt generation in the lower crust and the upper mantle might has been triggered by adiabatic decompression during orogen collapse.

CIZ post-kinematic felsic magmatism in the context of the western European Variscan Belt

Available geochronology of granites from the inner zones of the Iberian Variscan Collisional Belt (CIZ) points to a main felsic magmatic event in the broad range of 325–290 Ma, with its maximum about 313–298 Ma (Fig. 10). This relatively young age range (Westphalian to Permo-Carboniferous) indicates that the main episodes of Variscan granite plutonism in the CIZ coincide with thin-skinned thrusting in the foreland of the Cantabrian Zone (e.g. Pérez Estaún and Bastida 1990). In the case of the Eastern sector of the SCS Batholith, this large post-kinematic granite intrusions at 305–300 Ma took place within the Late Pennsylvanian (Kasimovian and Gzhelian stages; Davydov et al. 2010), during formation of the late-orogenic Stephanian coal basins in the Cantabrian Zone.

Though a detailed presentation of the Variscan magmatism is beyond the scope of this paper, it is worth noting that late- to post-kinematic granitoids from Western European Variscan massifs display intrusion ages which overlap the 313–298 Ma range of maximum magmatic activity in the CIZ (Fig. 10). The intrusion of large late-post-kinematic granitic plutons from the Armorican Massif (Ballèvre et al. 2009) is mainly constrained to the range 320–300 Ma. Post-tectonic felsic magmas in other southern Variscides tend to display similar or even younger ages, such as the French Massif Central (up to 290 Ma in the Velay dome; Ledru et al. 2001, and references therein), Pyrenees (312–305 Ma; Roberts et al. 2000 and references therein) or Calabria-Peloritani Massif (up to 295 Ma; Fiannacca et al. 2008 and references therein). In Corsica-Sardinia and the Alps, the post-tectonic felsic Variscan intrusions exhibit even younger emplacement ages (up to ~270 Ma; Dallagiovanna et al. 2009; Cocherie et al. 2005, and references therein).

The above studies demonstrate that large granitic bodies were emplaced along the western margin of the European Variscan Belt, in a late- to post-tectonic geodynamic setting, at the end of the Variscan collision (broadly from 315 to 290 Ma). Prior to ~320–330 Ma, granites from the above Variscan massifs are mostly syn-tectonic anatectic melts (e.g. Faure et al. 2010). Instead, granites emplaced during Namurian-Westphalian are late-orogenic intrusions associated with the extension and collapse of Variscan crust, which is a diachronous process that progressed from the internal zones outwards (e.g. Timmerman 2008 and references within). Further extension during Stephanian-early Permian is characterised by strike-slip faulting, which resulted in formation of intracontinental detrital basins accompanied by widespread post-orogenic volcanic and plutonic activity (e.g. Timmerman 2008). This protracted felsic magma generation event, related to the orogen collapse (younger than 320 Ma), seems to be coeval in all western Variscan massifs, though the more external areas display younger felsic magmas (e.g. Corsica-Sardinia and Alps). On the other hand, late Variscan granites from central Europe display slightly older ages (Klein et al. 2008) (Fig. 10).

Melting responsible of this late-orogenic magmatism in the western Variscides has been related to several geodynamic settings: lithospheric thinning and adiabatic decompression after continental collision (Schaltegger and Corfu 1995), break-off of subducted oceanic slab and thermal erosion of the lithospheric base (e.g. Schaltegger 1997) and roll-back effect of the Paleotethys subducting slab (Von Raumer et al. 2009). Many studies have stated that subduction of peri-Gondwana oceans (e.g. Rheic) was an active process until about 350 Ma and that after 355–345 Ma a collisional geodynamic setting dominate the western European Variscan Belt (e.g. Faure et al. 2009 for the French Massif Central; Ribeiro et al. 2010 for the Iberian Massif; and references included in these works). Even if subduction operated until 320 Ma, as suggested by Von Raumer et al. (2009) for the Paleotethys, the younger late-tectonic granitic magmatism of Western Europe should be associated with continental collision. Thermal models applied to thickened continental crusts suggest that an important increase in temperature at the lower crust might occur in a few 10s of million years after thickening.

This thermal input, together with the posterior lithospheric thinning, might explain the widespread crustal melting episode which characterises the upper Carboniferous-Permian transition in the western Variscides.

Conclusions

Zircon from five granitic intrusions from eastern Spanish Central System have been separated and analysed, using several analytical techniques, in order to characterise their trace element composition, determine their age of crystallisation and evaluate the source nature. Laser Ablation ICP-MS trace element data suggest that zircon composition varies mainly as a consequence of melt differentiation, although mixing with other felsic magmas is also occurring. The influence of co-precipitating accessory minerals, such as monazite, xenotime or allanite, can be deduced from the variation shown by zircon trace element composition with increasing degree of fractionation.

Four of the granite samples have a scarce number of pre-Variscan zircon cores. According to these inherited ages, a notorious difference between I- and S-type granites has been found. I-type intrusions display only Ordovician inherited grains in the restricted range of 479–462 Ma, though these early Palaeozoic relicts may also contain older zircon cores (pre-Cambrian). The Ordovician inheritances closely match the age of the widespread late Palaeozoic magmatism represented mainly by augen gneisses outcropping from northwest to central Spain. Thus, I-type plutons are likely derived from melting of Ordovician metaigneous protoliths. The sampled S-type granites display a more heterogeneous population of inherited zircons (all of them pre-Cambrian), which do not allow a straightforward interpretation regarding the nature of their protolith.

U-Th–Pb SHRIMP analyses of zircons from these granitic intrusions yielded exceedingly large apparent age ranges, which might be explained by a late magmatic Pb-loss event. This process caused rejuvenation of the zircon domains, so we have considered the highest apparent ages from these samples as the best approximation to the age of crystallisation. These ion microprobe data have been combined with U–Pb zircon ages obtained by TIMS and laser ablation ICP-MS, with the aim of making the calculated ages more robust. Our results suggest a relatively narrow range from 305 to 298 Ma for the intrusion of the five granitic bodies. Precise geochronological studies on granites from western SCS provided slightly older ages than those of eastern SCS. The absence of ages higher than 309 Ma in the SCS batholith reinforces its post-kinematic character and constrains its intrusion to a younger time span than previously thought. When comparing the intrusion ages of granites from the CIZ with those of near Variscan massifs, a widespread post-tectonic crustal melting episode seems to be apparent in the broad range of 315–290 Ma within the internal western Variscides.

Acknowledgments We acknowledge the constructive criticism of the anonymous editor and an anonymous referee, which greatly helped to improve the initial manuscript. This work is included in the objectives of, and supported by, the CGL-2008-05952 and the CGL2011-23560 projects of the Ministerio de Educación y Ciencia of Spain and the GR58/08 project of the 910492 UCM group.

References

Antunes IMHR, Neiva AMR, Silva MMVG, Corfu F (2008) Geochemistry of S-type granitic rocks from the reversely zoned Castelo Branco pluton (central Portugal). Lithos 103:445–465

Ballèvre M, Bosse V, Ducassou C, Pitra P (2009) Palaeozoic history of the Armorican Massif: models for the tectonic evolution of the suture zones. C R Geosci 341:174–201

Bea F, Montero P, Molina JF (1999) Mafic precursors, peraluminous granitoids, and late lamprophyres in the Avila batholith; a model for the generation of Variscan batholiths in Iberia. J Geol 107:399–419

Bea F, Montero P, Zinger T (2003) The nature, origin, and thermal influence of the granite source layer of Central Iberia. J Geol 111:579–595

Bea F, Montero P, González-Lodeiro F, Talavera C, Molina JF, Scarrow JH, Whitehouse MJ, Zinger T (2006) Zircon thermometry and U–Pb ion-microprobe dating of the gabbros and associated migmatites of the Variscan Toledo anatectic complex, central Iberia. J Geol Soc Lond 163:847–855

Bea F, Montero P, González-Lodeiro F, Talavera C (2007) Zircon inheritance reveals exceptionally fast crustal magma generation processes in central Iberia during the Cambro-Ordovician. J Petrol 48:2327–2339

Bellido F, Casillas R, Navidad M, De Pablo García JG, Peinado M, Villaseca C (1990) Las Navas del Marqués (532). Mapa Geol. Esp. 1:50,000 (segunda serie) IGME

Belousova EA, Griffin WL, O'Reilly SY, Fisher NI (2002) Igneous zircon: trace element composition as an indicator of source rock type. Contrib Miner Petrol 143:602–622

Belousova EA, Griffin WL, O'Reilly SY (2006) Zircon crystal morphology, trace element signatures and Hf isotope composition as a tool for petrogenetic modelling: examples from Eastern Australian granitoids. J Petrol 47:329–353

Bischoff L, Lenz H, Mueller P, Schmidt K (1978) Geochemical and geochronological investigations of metavolcanic rocks and orthogneiss in the eastern Sierra de Guadarrama, Spain. Neues Jahrb Geol Palaeo Abh 155:275–299

Black LP, Gulson BL (1978) The age of the Mud Tank carbonatite, Strangways Range, Northern Territory. BMR J Aust Geol Geophys 3:227–232

Black LP, Kamo SL, Allen CM, Aleinikoff JN, Davis DW, Korsch RJ, Foudoulis C (2003) TEMORA 1: a new zircon standard for phanerozoic U–Pb geochronology. Chem Geol 200:155–170

Black LP, Kamo SL, Allen CM, Davis DW, Aleinikoff JN, Valley JW, Mundil R, Campbell IH, Korsch RJ, Williams IS, Foudoulis C (2004) Improved $^{206}Pb/^{238}U$ microprobe geochronology by the monitoring of a trace-element-related matrix effect; SHRIMP, ID-TIMS, ELA-ICP-MS and oxygen isotope documentation for a series of zircon standards. Chem Geol 205:115–140

Carracedo M, Paquette JL, Alonso Olazabal A, Santos Zalduegui JF, García de Madinabeitia S, Tiepolo M, Gil Ibarguchi JI (2009) U–Pb dating of granodiorite and granite units of the Los Pedroches batholith. Implications for geodynamic models of the southern Central Iberian Zone (Iberian Massif). Int J Earth Sci 98:1609–1624

Casillas R, Vialette Y, Peinado M, Duthou JL, Pin C (1991) Âges et caractéristiques isotopiques (Sr, Nd) des granitoïdes de la Sierra de Guadarrama occidentale (Espagne). Abstract Séance Spécialisée Soc. Géol. France Mém. Jean Lameyre

Casquet C, Montero P, Bea F, Lozano R (2003) Geocronología $^{207}Pb/^{206}Pb$ en cristal único de circón y Rb–Sr del plutón de La Cabrera (Sierra de Guadarrama). Geogaceta 35:71–74

Castiñeiras P, Villaseca C, Barbero L, Martín Romera C (2008) SHRIMP U–Pb zircon dating of anatexis in high-grade migmatite complexes of Central Spain: implications in the Hercynian evolution of Central Iberia. Int J Earth Sci 97:35–50

Castro A, Patiño Douce AE, Corretgé LG, De la Rosa JD, El-Biad M, El-Hmidi H (1999) Origin of peraluminous granites and granodiorites, Iberian Massif, Spain. An experimental test to granite petrogenesis. Contrib Miner Petrol 135:255–276

Claiborne LL, Miller CF, Walker BA, Wooden JL, Mazdab FK, Bea F (2006) Tracking magmatic processes through Zr/Hf ratios in rocks and Hf and Ti zoning in zircons: an example from the Spirit Mountain batholith, Nevada. Miner Mag 70:517–543

Cocherie A, Rossi P, Fanning CM, Guerrot C (2005) Comparative use of TIMS and SHRIMP for U–Pb zircon dating of A-type granites and mafic tholeiitic layered complexes and dykes from the Corsican Batholith (France). Lithos 82:185–219

Dallagiovanna G, Gaggero L, Maino M, Seno S, Tiepolo M (2009) U–Pb zircon ages for post-Variscan volcanism in the Ligurian Alps (Northern Italy). J Geol Soc Lond 166:101–104

Davydov VI, Crowley JL, Schmitz MD, Poletaev VI (2010) High-precision U–Pb zircon age calibration of the global carboniferous time scale and the milankovitch band cyclicity in the Donets Basin, eastern Ukraine. Geochem Geophys Geosys 11:22

Dias G, Leterrier J, Mendes A, Simões PP, Bertrand JM (1998) U–Pb zircon and monazite geochronology of post-collisional Hercynian granitoids from the Central Iberian zone (northern Portugal). Lithos 45:349–369

Díaz-Alvarado J, Castro A, Fernández C, Moreno-Ventas I (2011) Assessing bulk assimilation in cordierite-bearing granitoids from the Central System Batholith, Spain: experimental, geochemical and geochronological constraints. J Petrol 52:223–256

Dunn AM, Reynolds PH, Clarke DB, Ugidos JM (1998) A comparison of the age and composition of the Sherburne Dyke, Nova Scotia, and the Messejana Dyke, Spain. Can J Earth Sci 35:1110–1115

Escuder-Viruete J, Hernáiz PP, Valverde P, Rodríguez R, Dunning G (1998) Variscan syncollisional extension in the Iberian Massif: structural, metamorphic and geochronological evidence from the Somosierra sector of the Sierra de Guadarrama (Central Iberian Zone, Spain). Tectonophysics 290:87–109

Faure M, Lardeaux J-M, Ledru P (2009) A review of the pre-permian geology of the Variscan French Massif Central. C R Geosci 341:202–213

Faure M, Cocherie A, Bé Mézème E, Charles N, Rossi P (2010) Middle carboniferous crustal melting in the Variscan Belt: new insights from U–Th–Pb_{tot} monazite and U–Pb zircon ages of the Montagne Noire Axial Zone (southern French Massif Central). Gondwana Res 18:653–673

Fernández-Suárez J, Dunning GR, Jenner GA, Gutiérrez-Alonso G (2000) Variscan collisional magmatism and deformation in NW Iberia: constraints from U–Pb geochronology of granitoids. J Geol Soc Lond 157:565–576

Fernández-Suárez J, Arenas R, Jeffries TE, Whitehouse MJ, Villaseca C (2006) A U–Pb study of zircons from a lower crustal granulite xenolith of the Spanish Central system: a record of Iberian lithospheric evolution from the Neoproterozoic to the Triassic. J Geol 114:471–483

Fernández-Suárez J, Gutierrez-Alonso G, Johnston ST, Jeffries TE, Pastor-Galán D, Jenner GA, Murphy JB (2011) Iberian late-Variscan granitoids: some considerations on crustal sources and the significance of "mantle extraction ages". Lithos 123:121–132

Ferreira E, Iglesias M, Noronha F, Pereira E, Ribeiro A, Ribeiro ML, Camicero A, Gonzalo JC, López-Plaza M, Rodríguez Alonso MD (1987) Granitoides da zona Centro-Ibérica e seu enquadramento geodinâmico. In: Bea F (ed) Geología de los granitoides y rocas asociadas del macizo Ibérico. Rueda, Madrid, pp 37–53

Ferry JM, Watson EB (2007) New thermodynamic models and revised calibrations for the Ti-in-zircon and Zr-in-rutile thermometers. Contrib Miner Petrol 154:429–437

Fiannacca P, Williams IS, Cirrincione R, Pezzino A (2008) Crustal contributions to late Hercynian peraluminous magmatism in the southern Calabria-Peloritani Orogen, southern Italy: petrogenetic inferences and the Gondwana connection. J Petrol 49:1497–1514

Finger F, Roberts MP, Haunschmid IB, Schermaier A, Steyrer HP (1997) Variscan granitoids of central Europe: their typology, potential sources and tectonothermal relations. Miner Petrol 61:67–96

Gagnevin D, Daly JS, Kronz A (2010) Zircon texture and chemical composition as a guide to magmatic processes and mixing in a granitic environment and coeval volcanic system. Contrib Miner Petrol 159:579–596

Galindo C, Huertas MJ, Casquet C (1994) Cronología Rb–Sr y K–Ar de diques de la Sierra de Guadarrama (Sistema Central Español). Geogaceta 16:23–26

Hoskin PWO, Schaltegger U (2003) The composition of zircon and igneous and metamorphic petrogenesis. In: Hanchar JM, Hoskin PWO (eds) Zircon: reviews in mineralogy and geochemistry, vol 53. Mineralogical Society of America, Washington, pp 27–62

Jackson SE, Pearson NJ, Griffin WL, Belousova EA (2004) The application of laser ablation-inductively coupled plasma-mass spectrometry to in situ U–Pb zircon geochronology. Chem Geol 211:47–69

Jaffey AH, Flynn KF, Glendenin LE, Bentley WC, Essling AM (1971) Precision measurement of half-lives and specific activities of ^{235}U and ^{238}U. Phys Rev 4:1889–1906

Julivert M, Fontboté JM, Ribeiro A, Navais-Conde LE (1972) Mapa tectónico de la Península Ibérica y Baleares a escala 1:1,000,000. Memoria explicativa. Spanish Geological Survey, Madrid, p 113

Klein T, Kiehm S, Siebel W, Shang CK, Rohrmüller J, Dörr W, Zulauf G (2008) Age and emplacement of late-Variscan granites of the western Bohemian Massif with main focus on the Hauzenberg granitoids (European Variscides, Germany). Lithos 102:478–507

Krogh TE (1973) A low-contamination method for hydrothermal decomposition of zircon and extraction of U and Pb for isotopic age determinations. Geochim Cosmochim Acta 37:485–494

Ledru P, Courrioux G, Dallain C, Lardeaux JM, Montel JM, Vanderhaeghe O, Vitel G (2001) The Velay dome (French Massif Central): melt generation and granite emplacement during orogenic evolution. Tectonophysics 342:207–237

Linnen RL, Keppler H (2002) Melt composition control of Zr/Hf fractionation in magmatic processes. Geochim Cosmochim Acta 66:3293–3301

Ludwig KR (1991) PBDAT: a computer program for processing Pb–U–Th isotope data, version 1.24: a user's manual. Berkeley Geochronological Center, open-file report 88–542

Ludwig KR (2001) SQUID 1.02, a user's manual. Berkeley Geochronological Center, special publication no 2, pp 1–17

Ludwig KR (2003) ISOPLOT/Ex, version 3: a geochronological toolkit for Microsoft Excel. Berkeley Geochronological Center, special publication no 4, pp 1–71

Macaya J, González-Lodeiro F, Martínez-Catalán JR, Álvarez F (1991) Continuous deformation, ductile thrusting and backfolding of cover and basement in the Sierra de Guadarrama, Hercynian orogen of central Spain. Tectonophysics 191:291–309

Martins HCB, Sant'Ovaia H, Noronha F (2009) Genesis and emplacement of felsic Variscan plutons within a deep crustal lineation, the Penacova–Régua–Verín fault: an integrated geophysics and geochemical study (NW Iberian Peninsula). Lithos 111:142–155

Matte P (1986) Tectonics and plate tectonic model for the Variscan Belt of Europe. Tectonophysics 126:331–334

Matte P (2001) The Variscan collage and orogeny (480 ± 290 Ma) and the tectonic definition of the Armorica microplate: a review. Terra Nova 13:122–128

Mattinson JM (2005) Zircon U–Pb chemical abrasion ("CA-TIMS") method: combined annealing and multi-step partial dissolution analysis for improved precision and accuracy of zircon ages. Chem Geol 220:47–66

Miller CF, McDowell SM, Mapes RW (2003) Hot and cold granites? Implications of zircon saturation temperatures and preservation of inheritance. Geology 31:529–532

Montero P, Bea F, Zinger T (2004) Edad $^{207}Pb/^{206}Pb$ en cristal único de circón de las rocas máficas y ultramáficas del sector de Gredos, batolito de Ávila (Sistema Central Español). Revista de la Sociedad Geológica de España 17:157–167

Montero P, Talavera C, Bea F, Lodeiro FG, Whitehouse MJ (2009) Zircon geochronology of the Ollo de Sapo formation and the age of the Cambro-Ordovician rifting in Iberia. J Geol 117:174–191

Moreno-Ventas I, Rogers G, Castro A (1995) The role of hybridization in the genesis of the Hercynian granitoids in the Gredos Massif, Spain: inferences from Sr–Nd isotopes. Contrib Miner Petrol 120:137–149

Neiva AMR, Williams IS, Ramos JMF, Gomes MEP, Silva MMVG, Antunes IMHR (2009) Geochemical and isotopic constraints on the petrogenesis of early Ordovician granodiorite and Variscan two-mica granites from the Gouveia area, central Portugal. Lithos 111:186–202

Orejana D, Villaseca C, Billström K, Paterson BA (2008) Petrogenesis of Permian alkaline lamprophyres and diabases from the Spanish Central System and their geodynamic context within Western Europe. Contrib Miner Petrol 156:477–500

Orejana D, Villaseca C, Pérez-Soba C, López-García JA, Billström K (2009) The Variscan gabbros from the Spanish Central System: a case for crustal recycling in the sub-continental lithospheric mantle? Lithos 110:262–276

Orejana D, Villaseca C, Armstrong RA, Jeffries TE (2011) Geochronology and trace element chemistry of zircon and garnet from granulite xenoliths: constraints on the tectonothermal evolution of the lower crust under central Spain. Lithos 124:103–116

Pérez Estaún A, Bastida F (1990) Pre-mesozoic geology of Iberia. In: Dallmayer RD, Martínez García E (eds) Pre-mesozoic geology of Iberia. Springer, Berlin, pp 55–69

Pérez-Soba C, Villaseca C, González del Tánago J, Nasdala L (2007) The composition of zircon in the Hercynian peraluminous granites of the Spanish Central System batholith. Can Miner 45:509–527

Pidgeon RT, Nemchin AA, Hitchen GJ (1998) Internal structures of zircons from Archaean granites from the Darling Range batholith: implications for zircon stability and the interpretation of zircon U–Pb ages. Contrib Miner Petrol 132:288–299

Pinarelli L, Rottura A (1995) Sr and Nd isotopic study and Rb–Sr geochronology of the Béjar granites, Iberian Massif, Spain. Eur J Miner 7:577–589

Pupin JP (2000) Granite genesis related to geodynamics from Hf–Y in zircon. Edinb Geol Soc Trans Earth Sci 91:245–256

Ribeiro A, Munhá J, Fonseca PE, Araújo A, Pedro JC, Mateus A, Tassinari C, Machado G, Jesus A (2010) Variscan ophiolite belts in the Ossa-Morena zone (southwest Iberia): geological characterization and geodynamic significance. Gondwana Res 17:408–421

Roberts MP, Pin C, Clemens JD, Paquette JL (2000) Petrogenesis of mafic to felsic plutonic rock associations: the calc-alkaline Quérigut complex, French Pyrenees. J Petrol 41:809–844

Scarrow JH, Bea F, Montero P, Molina JF, Vaughan APM (2006) A precise late Permian $^{40}Ar/^{39}Ar$ age for Central Iberian camptonitic lamprophyres. Geol Acta 4:451–459

Scarrow JH, Molina JF, Bea F, Montero P (2009) Within-plate calc-alkaline rocks: insights from alkaline mafic magma–peraluminous crustal melt hybrid appinites of the Central Iberian Variscan continental collision. Lithos 110:50–64

Schaltegger U (1997) Magma pulses in the central Variscan Belt: episodic melt generation and emplacement during lithospheric thinning. Terra Nova 9:242–245

Schaltegger U, Corfu F (1995) Late Variscan "basin and range" magmatism and tectonics in the Central Alps: evidence from U–Pb geochronology. Geodin Acta 8:82–98

Serrano Pinto M, Casquet C, Ibarrola E, Corretgé LG, Portugal Ferreira M (1987) Sintese geocronologica dos granitoides do Maciço Hesperico. In: Bea F, Camicero A, Gonzalo JC, López Plaza M, Rodríguez Alonso MD (eds) Geología de los granitoides y rocas asociadas del Macizo Hespérico. Rueda, Madrid, pp 69–86

Solá AR, Williams IS, Neiva AMR, Ribeiro ML (2009) U–Th–Pb SHRIMP ages and oxygen isotope composition of zircon from two contrasting late Variscan granitoids, Nisa-Albuquerque batholith, SW Iberian Massif: petrologic and regional implications. Lithos 111:156–167

Stacey JS, Kramers JD (1975) Approximation of terrestrial lead isotope evolution by a two-stage model. Earth Planet Sci Lett 26:207–221

Sun SS, McDonough WF (1989) Chemical and isotopic systematics of oceanic basalts; implications for mantle composition and processes. In: Saunders AD, Norrey MJ (eds) Magmatism in ocean basins. Blackwell, geological society of special publication no 42, Oxford, pp 313–345

Teixeira RJS, Neiva AMR, Silva PB, Gomes MEP, Andersen T, Ramos JM (2011) Combined U–Pb geochronology and Lu–Hf isotope systematics by LAM–ICPMS of zircons from granites and metasedimentary rocks of Carrazeda de Ansiães and Sabugal areas, Portugal, to constrain granite sources. Lithos 125:321–334

Timmerman MJ (2008) Palaeozoic magmatism. In: McCann T (ed) The geology of Central Europe, vol 1. Precambrian and Palaeozoic. Geol Soc Lond, pp 665–748

Ugidos JM, Recio C (1993) Origin of cordierite-bearing granites by assimilation in the Central Iberian zone, Spain. Chem Geol 103:27–43

Valle Aguado B, Azevedo MR, Schaltegger U, Martínez-Catalán JR, Nolan J (2005) U–Pb zircon and monazite geochronology of Variscan magmatism related to syn-convergence extension in Central Northern Portugal. Lithos 82:169–184

Valverde-Vaquero P (1998) An integrated field, geochemical and U–Pb geochronological study of the southwest hermitage flexure (Newfoundland Appalachians, Canada) and the Sierra de Guadarrama (Iberian Massif, central Spain): a contribution to the understanding of the geological evolution of circum-Atlantic

peri-Gondwana. PhD thesis, Memorial University of Newfoundland, Canada

Valverde-Vaquero P, Dunning GR (2000) New U–Pb ages for early Ordovician magmatism in Central Spain. J Geol Soc Lond 157:15–26

Valverde-Vaquero P, Dörr W, Belka Z, Franke W, Wiszniewska J, Schastok J (2000) U–Pb single-grain dating of detrital zircon in the Cambrian of central Poland: implications for Gondwana versus Baltica provenance studies. Earth Planet Sci Lett 184:225–240

Valverde-Vaquero P, Díez-Balda MA, Díez-Montes A, Dörr W, Escuder-Viruete J, Gonzalez-Clavijo E, Maluski H, Rodríguez-Fernández LR, Rubio F, Villar P (2007) The "hot orogen": two separate Variscan low-pressure metamorphic events in the Central Iberian zone. Geol de la France 2007:168

Villaseca C, Barbero L (1994) Estimación de las condiciones de metamorfismo hercínico de alta presión de la Sierra de Guadarrama. Geogaceta 16:27–30

Villaseca C, Herreros V (2000) A sustained felsic magmatic system: the Hercynian granitic batholith of the Spanish Central System. Edinb Geol Soc Trans Earth Sci 91:207–219

Villaseca C, Eugercios L, Snelling LJ, Huertas MJ, Castellón T (1995) Nuevos datos geocronológicos (Rb–Sr, K–Ar) de granitoides hercínicos de la Sierra de Guadarrama. Revista de la Sociedad Geológica de España 8:129–140

Villaseca C, Barbero L, Rogers G (1998) Crustal origin of Hercynian peraluminous granitic batholiths of central Spain: petrological, geochemical and isotopic (Sr, Nd) arguments. Lithos 43:55–79

Villaseca C, Downes H, Pin C, Barbero L (1999) Nature and composition of the lower continental crust in central Spain and the granulite-granite linkage: inferences from granulitic xenoliths. J Petrol 40:1465–1496

Villaseca C, Orejana D, Pin C, López García JA, Andonaegui P (2004) Le magmatisme basique hercynien et post-hercynien du Système Central Espagnol: essai de caractèrisation des sources mantelliques. C R Géosci 336:877–888

Villaseca C, Bellido F, Pérez-Soba C, Billström K (2009) Multiple crustal sources for post-tectonic I-type granites in the Hercynian Iberian belt. Miner Petrol 96:197–211

Villaseca C, Orejana D, Belousova E, Armstrong RA, Pérez-Soba C, Jeffries TE (2011) U–Pb isotopic ages and Hf isotope composition of zircons in Variscan gabbros from central Spain: evidence of variable crustal contamination. Miner Petrol 101:151–167

Von Raumer JF, Bussy F, Stampfli GM (2009) The Variscan evolution in the external massifs of the Alps and place in their Variscan framework. C R Geosci 341:239–252

Wiedenbeck M, Alle P, Corfu F, Griffin WL, Meier M, Oberli F, Von Quadt A, Roddick JC, Spiegel W (1995) Three natural zircon standards for U–Th–Pb, Lu–Hf, trace element and REE analyses. Geostand Newslett 19:1–23

Williams IS (1998) U–Th–Pb geochronology by ion microprobe. In: McKibben MA, Shanks WCP, Ridley WI (eds) Applications of microanalytical techniques to understanding mineralizing processes. Rev Econ Geol 7:1–35

Zeck HP, Wingate MTD, Pooley GD, Ugidos JM (2004) A sequence of Pan-African and Hercynian events recorded in zircons from an orthogneiss from the Hercynian belt of western central Iberia—an ion microprobe U–Pb study. J Petrol 45:1613–1629

Zeck HP, Whitehouse MJ, Ugidos JM (2007a) 496 ± 3 Ma zircon ion microprobe age for pre-Hercynian granite, Central Iberian zone, NE Portugal (earlier claimed 618 ± 9 Ma). Geol Mag 144:21–31

Zeck HP, Wingate MTD, Pooley G (2007b) Ion microprobe U–Pb zircon geochronology of a late tectonic granitic–gabbroic rock complex within the Hercynian Iberian belt. Geol Mag 144:157–177